2021-08

# Clay-based ceramic materials for water de-fluorida

Leonidas, Wilson

NM-AIST

# CLAY-BASED CERAMIC MATERIALS FOR WATER DE-FLUORIDATION

**Wilson Leonidas**

**A Dissertation Submitted in Partial Fulfillment of the Requirements for the Degree of Master's in Materials Science and Engineering of the Nelson Mandela African Institution of Science and Technology**

**Arusha Tanzania**

**August, 2020**

## ABSTRACT

Long-term consumption of water with fluoride concentration above the WHO recommended limit of 1.5 mg/g may cause fluorosis. Low-income communities living in fluoride endemic regions are more affected as they cannot afford well-established water de-fluoridation technologies. Currently, clay ceramic materials impregnated with silver colloids have been used to disinfect water disregarding the removal of fluoride. This work investigated improving the de-fluoridation capacity of clay ceramic materials with in-situ generated Ca/Mg phosphate system using locally available carbonate rocks as a source of Ca/Mg. To achieve this, clay-Ca/Mg phosphate system composite ceramic materials were synthesized from varied ratios of clay (K) to carbonate rock materials (R) (K:R = 0:100, 90:10, 85:15, 75:25 and 100:0), sintered at various temperatures between 500 ℃ and 900 ℃. The materials were characterized using XRF, FTIR, AAS, CHNS-O analyzer and X-ray PDF analysis. The three types of carbonate rock materials investigated were identified to be; high-calcium limestone, magnesium-deficient dolomite and near-stoichiometric dolomite. The magnesium-deficient dolomite gave rise to a Ca/Mg phosphate system that exhibited superior de-fluoridation performance. The material improved in de-fluoridation performance with increase sintering temperature from 500 ℃ to 700 ℃, possibly due to an increase in the more soluble magnesium-substituted tri-calcium phosphate (β-$Mg_xCa_{3-x}PO_4$), CaO and MgO (PDF and FTIR). This work has shown that the de-fluorination performance of clay ceramic materials can be improved with a phosphate system synthesized/formed in-situ using carbonate rocks as Ca/Mg source. The method of improving the de-fluoridation performance of clay ceramic materials introduced in this present study has potential applications in the fabrication of water filters with fluoride removal ability.

## DECLARATION

I, Wilson Leonidas**,** do hereby declare to the Senate of The Nelson Mandela African Institution of Science and Technology that this dissertation is my own original work and that it has neither been submitted nor being concurrently submitted for degree award in any other institution.

**Wilson Leonidas**

| **(Candidate name)** | **Signature** | **Date** |
|---|---|---|

The above declaration is confirmed,

**Prof. Revocatus Machunda**

| **(Supervisor 1)** | **Signature** | **Date** |
|---|---|---|

**Dr. Askwar Hilonga**

| **(Supervisor 2)** | **Signature** | **Date** |
|---|---|---|

## COPYRIGHT

## CERTIFICATION

The undersigned certify that they have read and hereby recommend for acceptance by The Nelson Mandela African Institution of Science and Technology a dissertation entitled *Clay-Based Ceramic Materials for Water De-fluoridation* in fulfillment of the requirement for the degree of Master's in Materials Science and Engineering of The Nelson Mandela African Institution of Science and Technology.

**Prof. Revocatus Machunda**

| **(Supervisor 1)** | **Signature** | **Date** |
|---|---|---|

**Dr. Askwar Hilonga**

| **(Supervisor 2)** | **Signature** | **Date** |
|---|---|---|

## ACKNOWLEDGEMENT

This work would not have been possible without the scholarship funding of African Development Bank. I am also grateful to my supervisors, Prof. Revocutus Machunda and Dr. Askwar Hilonga for their supportive guidance. Their guidance and encouragement played a pivotal role in making this work a success. I also thank NM-AIST for granting me a study leave.

It would be unfair not to mention the support of the University of Columbia (in the USA) through Bilinge group for assisting with the x-ray characterization of some of the materials used in this study.

## DEDICATION

This work is dedicated to my wife Claudia A. Mahene and my children (Alexander Mahene, Andrew Mahene, Clara Mahene and Innocent Mahene).

## TABLE OF CONTENTS

## LIST OF TABLES

## LIST OF FIGURES

## LIST OF ABBREVIATIONS AND SYMBOLS

| | |
|---|---|
| AAS | Atomic absorption spectroscopy (AAS) |
| ACP | Amorphous calcium phosphate |
| BBOT | 2,2'-(2,5-Thienediyl)bis[5-(2-methyl-2-propanyl)-1,3-benzoxazole] |
| CPP | Calcium pyrophosphate |
| $Q_m$ | De-fluoridation capacity (or maximum adsorption Capacity) |
| DO | Dissolved Oxygen |
| EC | Electrical conductivity |
| FTIR | Fourier-transform infrared spectroscopy |
| MgCPP | Magnesium substituted calcium pyrophosphate |
| MgOCP | Magnesium substituted octacalcium |
| N/A | Not applicable |
| OCP | Octacalcium phosphate |
| ORP | Oxidation-reduction potential |
| PDF | The atomic pair distribution function |
| R*w* | Residual factor |
| TGA | Thermogravimetric analysis |
| TISAB II | Total ionic adjustment buffers II |
| $U_{iso}$ | Sotropic displacement parameter |
| WHO | World Health Organization |
| βMgTCP | Beta magnesium-substituted tricalcium phosphate |
| βTCP | Beta tricalcium phosphate |

# CHAPTER ONE

# INTRODUCTION

## 1.1 Background of the Problem

Africa harbors two of the five major fluoride ($F^-$) belts in the world; the Northern African Belt and the Great Rift Valley belt. These belts release fluoride into groundwater to elevated levels. Persistent drought that characterizes the climate of the great East African Rift Valley (EARV) has forced inhabitants to rely on groundwater from these fluoride-rich beds. Consumption of water with fluoride concentration 0.5 – 1 mg/L is beneficial for the prevention of dental caries, but excessive consumption >1.5 mg/L can lead to health problems such as dental and skeletal fluorosis with neurological complications (Ajayi & Lamidi, 2015; Rango, Vengosh, Jeuland, Whitford, & Tekle-Haimanot, 2017). Geogenic $F^-$ contamination of groundwater is a major problem, rendering over 80 million people inhabiting EARV prone to Fluorosis. Globally the problem affects over 200 million people (Amini *et al.*, 2008). De-fluoridation has been used as an alternative means of providing safe drinking water (Yadav, Gupta, Kumar, Khan, & Kumar, 2018).

There are many high-tech water de-fluoridation technologies in existence. They include membrane separation (reverse osmosis), ion exchange resin, electrocoagulation and electrodialysis. However, these well-established technologies are too expensive to be accessed by communities in low-income settings, as they require high initial investment and running cost (Sobsey, Stauber, Casanova, Brown & Elliott, 2008; Zereffa & Bekalo, 2017). They also require electricity, which is either unavailable or inaccessible to many low-income households, particularly those in rural areas.

Owing to their affordability and straightforwardness, both in outline and application, and non-requirement of electricity, technologies based on adsorption appear to be the appropriate method in these settings. Adsorption technologies such as bone char filtration, calcium phosphate systems, locally available adsorbent geo-materials and combination systems employing chemical coagulation-flocculation may be used.

Clay ceramic filters are currently in use in many parts of East-Africa, including Tanzania. While clay ceramic filters are effective for removal of microorganisms, they have shown limited fluoride adsorption and other charged properties due to low affinity for the

contaminants (Erhuanga, Kashim, & Akinbogun, 2014; Shivaraju, Egumbo, Madhusudan, Anil Kumar, & Midhun, 2018; Svinka, Svinka, Pudze, & Damberga, 2015). To improve the de-fluoridation performance of clay ceramic filters, a few researchers have attempted to incorporate some additives known to have high fluoride adsorption. Agarwal, Rai, Shrivastav, and Dass (2003) observed that amending clay ceramic materials with Ca (as pure $CaCO_3$), Fe (as $FeCl_3$), or Al (as activated $Al_2O_3$) improved de-fluoridation performance in the same order. Elsewhere, Yakub and Soboyejo (2013) incorporated hydroxylapatite (calcium phosphate system), synthesized using reagent grade calcium hydroxide ($Ca(OH)_2$) as a calcium source. The resultant filter proved effective in the removal of both fluoride and bacteria. However, the purification of the additives or precursor materials is both costly and technically demanding. This calls for research to investigate the feasibility of replacing reagent grade materials with locally mined impure geo-materials to eliminate the need for pre-purification, hence potentially reducing the cost associated with the production of the resultant filters.

Since carbonate rocks are locally abundantly available, they can replace pure $Ca(OH)_2$ in the synthesis of $F^-$ adsorbing calcium phosphate systems to incorporate in clay ceramic filters. Also, since clay may contain compounds that can act as sources of cations, *in-situ* synthesis of phosphate systems could be a viable incorporation method.

This work is a continued effort to synthesize calcium phosphate system incorporated ceramic with desirable properties for water de-fluoridation. The current study aims to investigate the feasibility of synthesizing clay ceramic materials containing *in-situ* formed calcium phosphate system using carbonate rocks as a calcium source for water de-fluoridation. The synthesis method that will be devised in this work has potential applications in the fabrication of ceramic filters capable of removing both fluoride and pathogenic microbes.

## 1.2 Statement of the Problem

Ceramic water filtration is one of the low-cost water treatment methods from local materials. In many parts of East Africa, clay ceramic filters are used for water filtration. However, while clay ceramics are effective for the removal of microorganisms, they have shown limited removal efficiency for fluoride due to low affinity for the contaminant (Svinka *et al.*, 2015; Yakub & Soboyejo, 2013). Previous researches have incorporated pure reagent-grade additives such as Ca (as pure $CaCO_3$), Fe (as $FeCl_3$), Al (as activated $Al_2O_3$) and hydroxylapatite (Agarwal *et al.*, 2003; Yakub & Soboyejo, 2013). However, the purification of the additives or

precursor materials is both costly and technically demanding. This calls for research attention to investigate the feasibility of replacing reagent grade materials with locally mined impure geo-materials to eliminate the need for pre-purification, hence potentially reducing the cost associated with the production of the resultant filters. The current study will investigate the feasibility of improving the de-fluoridation performance of clay ceramics with *in-situ* generated phosphate system using locally available carbonate rocks as sources of calcium/magnesium.

## 1.3 Rationale of the Study

In East Africa, clay ceramic materials have been used to disinfect water disregarding the removal of fluoride, which is an ion of major health concern in fluoride endemic regions. The use of established fluoride removal methods is limited by its high cost, there is a need to develop affordable technologies. One method is to incorporate de-fluoridating agents in the ceramic filter matrix using readily available materials. This study investigates the feasibility of improving de-fluoridation capacity of clay ceramic materials with in-situ generated Ca/Mg phosphate system using locally available carbonate rocks as a source of Ca/Mg.

## 1.4 Objectives

### 1.4.1 General Objective

Development of clay ceramic materials, containing in-situ generated calcium/magnesium phosphate system, for water de-fluoridation, from locally available clay and carbonate rock materials.

### 1.4.2 Specific Objectives

(i) To synthesize clay-Ca/Mg phosphate composite ceramic materials, and optimize ingredient ratios and sintering temperatures.

(ii) To study thermodynamics and kinetic adsorption behavior of the synthesized material.

(iii) To study the renewability of the material.

## 1.5 Research Questions

(i) What is the potentiality of using carbonate rocks as a source of cations in the synthesis of clay-Calcium phosphate composite ceramic materials with water de-fluoridation ability?

(ii) Can calcium phosphate system be incorporated in porous clay-ceramic by in-situ synthesis?

(iii) What is the optimum ingredient (precursor materials) ratio and firing temperatures for the preparation of a clay-Ca/Mg phosphate composite ceramic that exhibits high de-fluoridation activity?

(iv) How can the synthesized ceramic materials, used for water purification, be regenerated?

## 1.6 Significance of the Study

To provide new alternative materials, based on locally available precursors, for water purification. The study has the potential of broadening the water decontamination spectrum of clay ceramic filters to include de-fluoridation, thereby providing safe drinking water to low-income communities living in fluoride endemic settings.

## 1.7 Delineation of the Study

In this study, clay ceramic materials containing in-situ formed calcium/magnesium phosphate system was synthesized using dolostone (magnesium deficient dolomite and near-stoichiometric dolomite) and limestone as sources of calcium and magnesium. The fluoride removal performance, kinetics and renewability (regeneration) of the synthesized ceramic composite was studied.

# CHAPTER TWO

# LITERATURE REVIEW

## 2.1 Clay Based Ceramic Materials in Water De-Fluoridation, Current Status

Clay ceramics are known to exhibit adsorptive properties that allow their use in water treatment processes. Sorption properties can vary over a wide range, depending on the mineralogical and chemical composition of clay, type of additives, firing temperature, porosity and the specific surface area of pores. Locally fabricated clay ceramic filters for water purification are in use in many parts of East Africa, including Tanzania. However, although these filters (which are single ceramic piece filters) are effective in the removal of microbes, they have shown limited water de-fluoridation performance. Hauge, Österberg, Bjorvatn, and Selvig (1994) observed that about 1 g of clay ceramic materials sintered at 600 °C could de-fluoridate 10 mL of fluoride water from 10 mg/L to approximately 2 mg/L. This means that over 1 Kg of ceramic materials would be required to de-fluoridate 10 L of water (with $F^-$ concentration of 10 mg/L) in 12 hours. The performance can be lower than that depending on the composition of the clay material. The poor de-fluoridation performance is caused by limited adsorption properties that ceramic materials have. To improve the de-fluoridation performance of clay ceramic materials, a few researchers have attempted to incorporate some additives known to have high fluoride adsorption. Agarwal *et al.* (2003) observed that amending clay ceramic materials with Ca (as pure $CaCO_3$), Fe (as $FeCl_3$) or Al (as activated $Al_2O_3$) improved de-fluoridation performance in the same order. Elsewhere, Yakub and Soboyejo (2013) incorporated hydroxylapatite (calcium phosphate system), synthesized using reagent grade $Ca(OH)_2$ as a calcium source. The resultant filter proved effective in the removal of both fluoride and bacteria. However, the purification of the additives or precursor materials is both costly and technically demanding. This calls for research attention to investigate the feasibility of replacing reagent grade materials with locally mined impure geo-materials to eliminate the need for pre-purification, hence potentially reducing the cost associated with the production of the resultant filters.

Since carbonate rocks are locally abundantly available, they can replace pure $Ca(OH)_2$ in the synthesis of $F^-$ adsorbing calcium phosphate systems for incorporating in the clay ceramic filters. Also, since clay may contain compounds that can act as sources of cations, *in-situ* synthesis of phosphate systems could be a viable incorporation method. In the current study, locally available carbonate rock materials (impure material) will be used as a Ca/Mg source in

the synthesis of clay ceramic materials containing *in-situ* generated phosphate system for water purification.

## 2.2 Clays and Clay Minerals (Hydrous Aluminum Phyllosilicates)

There are many types of clay and clay minerals. To be able to select the appropriate type of clay for the fabrication of a ceramic piece with desired properties for a particular application, understanding the properties of clay minerals and clays is critical. It is for this reason that this section dwells on the definition, classification and application suitability of clay minerals/clays. A brief description of fabrication methods and thermal properties of clay minerals is also provided.

### 2.2.1 What are Clays and Clay Minerals?

According to soil literature, the term clay denotes a class of various minerals consisting of particles with an equivalent spherical diameter of less than 2 μm (Theng, 2012). This definition is based on texture and particle size, rather than the chemical composition and mineralogical structure of the particles. In this work, the definition of clay emphasizes the presence of hydrous aluminum phyllosilicate minerals (clay minerals) in quantities enough to impart plasticity (hydroplasticity) on earth materials upon addition of an appropriate amount of water. In the context of this work, therefore, clays are earth materials containing hydrous aluminum phyllosilicate minerals, which upon addition of an appropriate amount of water become plastic and moldable. Other minerals that may be present in varying quantities are such as quartz, carbonates and metal oxides.

Aluminum phyllosilicates (phyllon - leaf) are silicate minerals with leaf-like or plate-like structure made up of two kinds of horizontal sheets; a tetrahedron silicon sheet and an alumina octahedron. Tetrahedron silicon sheet is an interlocking array or a series of these silica tetrahedra tied together horizontally by shared oxygen anions give a tetrahedral sheet (Bergaya & Lagaly, 2013; Guggenheim *et al.*, 2006). The alumina octahedron: Aluminum and/or magnesium ions are the key cations surrounded by six oxygen atoms or hydroxyl groups giving an eight-sided building block termed octahedron (Guggenheim *et al.*, 2006; Moore & Reynolds, 1989; Murray, 1999).

### 2.2.3 Classification of Clay Minerals

The hydrous aluminum phyllosilicates (clay minerals) are divided based on the layer type and the structural chemical composition within the layer. Two types of layers, depending on the component sheets, are a '1:1 layer' consisting of a tetrahedral (T) sheet and an octahedral sheet (O), and a '2:1 layer' containing two tetrahedral sheets sandwiching an octahedral sheet (Guggenheim *et al.*, 2006; Valášková & Martynková, 2012). Some of the common clay mineral kaolinite, smectite, vermiculite, illite (or mica-like) and chlorite. Figure 1 is a pictorial presentation of how the sheets and layers are arranged in clay minerals.

(i) Kaolinite is a two-sheet mineral (1:1) with the general formula $Al_2Si_2O_5(OH)_4$. Mineral units (unit structures) are firmly held together by hydrogen bonding to such that even water is restricted from entering the inter-layer spaces. This limits swelling upon addition of water (Guggenheim *et al.*, 2006; Kadir & Akbulut, 2009; Ombaka, 2016; Ugolini, Dahlgren, LaManna, Nuhn & Zachara, 1991). Low swelling and shrinkage due to limited water absorption make kaolinite less susceptible to cracks during drying and sintering, and therefore the preferred type of clay for the ceramic industry (Olaremu, 2015).

(ii) Smectite is a 2:1 layers mineral (an octahedral sheet (O) between two silica tetrahedral sheets (T); T-O-T structure) with inter-layers bonded by Van der Waals forces making the layers easily separated by absorption of water into the interlayer and other polar liquids (Bergaya & Lagaly, 2013).

(iii) Illite minerals are three-sheet (2:1) mineral, an octahedral sheet sandwiched between two silica tetrahedral sheets (T-O-T structure) where units are bound together by fixed or exchangeable cations (Bergaya & Lagaly, 2013). Illite clay mineral belongs to a subgroup mica called clay micas (Bergaya & Lagaly, 2013; Gualtieri *et al.*, 2008). It is non-expansive because the interlayer space is filled with poorly hydrated potassium or calcium and magnesium ions which hinder water molecules from intercalating (Bergaya & Lagaly, 2013). On comparison, Illite can absorb more water than kaolinite, although much less than montmorillonite.

(iv) Chlorite minerals are hydrous aluminosilicates with the basic structure 2:1 layers (two silica sheets sandwiching octahedral gibbsite or brucite sheet = T-O-T) with an interlayer (Bergaya & Lagaly, 2013). Unlike other T-O-T clay minerals whose

interlayer spaces are occupied by cations, chlorite minerals have their interlayer spaces occupied by $(Mg^{2+}, Fe^{3+})(OH)_6$, a unit that resembles brucite mineral $(Mg(OH)_2$ and which is commonly referred to as the brucite-like layer (Bergaya & Lagaly, 2013).

(v) Vermiculite is a hydrated magnesium aluminum-iron silicate which possesses 2:1 type of clay minerals (TOT structure) (Guggenheim *et al.*, 2006). The massive thermal expansion of vermiculite during thermal sintering causes cracking of the objects fabricated with clays containing high vermiculite content (Okada, Matsui, Isobe, Kameshima & Nakajima, 2008).

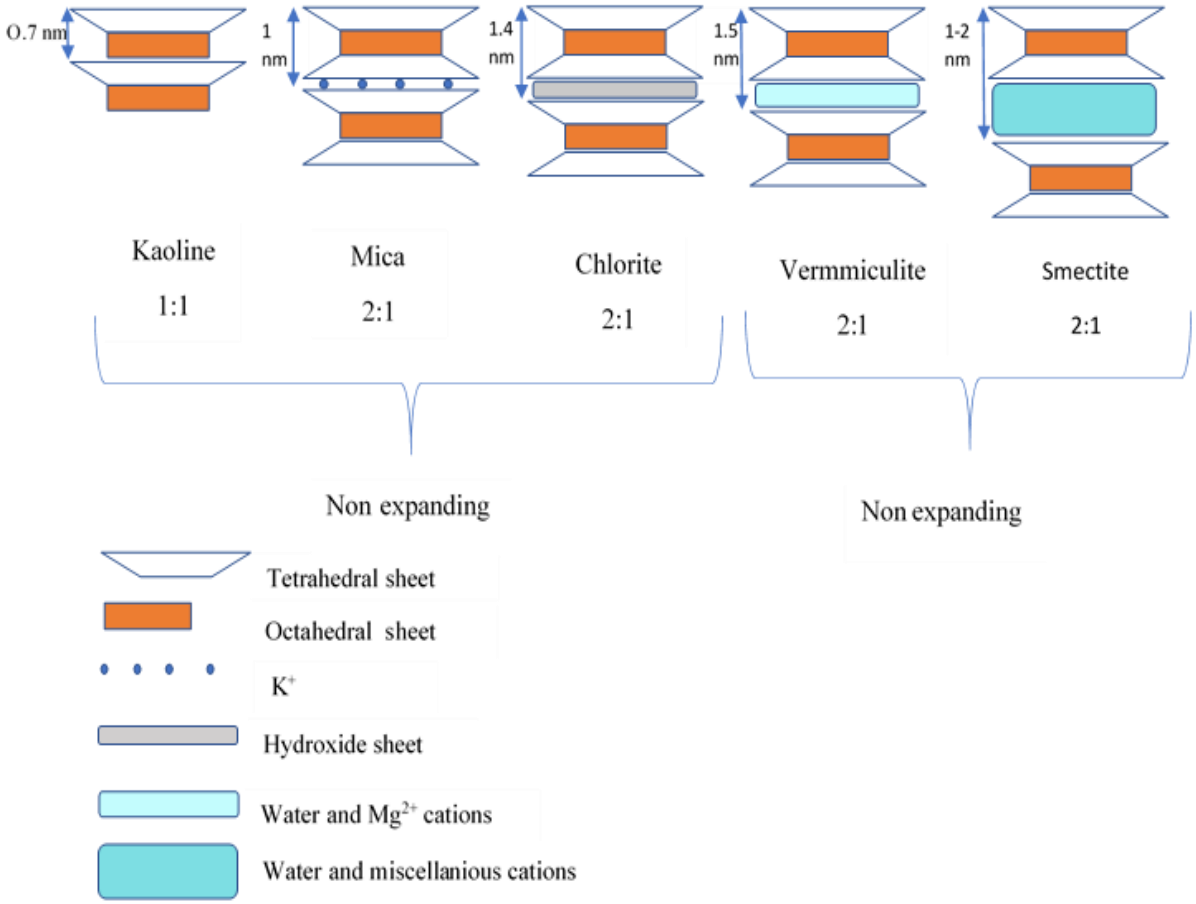


**Figure 1: Classification of clay minerals (Hydrous Aluminum phyllosilicates**

### 2.2.3 Fabrication, Drying and Thermal Sintering of Clay Products

Ground clay materials may be shaped into greenware of the object of the targeted final ceramic piece. This can be achieved by either hydroplastic forming or slip casting. In the former technique, an appropriate amount of water is added to make it plastic enough to mold or extrude

through a hollow object (mold). In the later (slip casting), water suspended clay material is poured into a porous mold with the shape of the intended object (William & Rethwisch, 2009).

The greenware needs to dry before firing. As a clay-based ceramic body dries, it also experiences some shrinkage. While drying at the surface of the body is controlled by evaporation, the interior dries through diffusion of water to the surrounding surface (William & Rethwisch, 2009). If the rate of evaporation is greater than the rate of diffusion, the surface will dry and as a consequence shrink more rapidly than the interior, leading to crack formation. The rate of surface evaporation should, therefore, be diminished to the rate of water diffusion; evaporation rate can be controlled by temperature, humidity and the rate of airflow (William & Rethwisch, 2009). For some clay minerals such as smectites, the effect is so pronounced that it limits their use in ceramic shape fabrication. Smectites lose the adsorbed water rapidly during dehydration. Due to the differential rate of loss of water between the surface and the inner part, clay green body made from smectites crack as they dry, posing a challenge in ceramic shape fabrication (Vasić, Pezo, Zdravković, Bačkalić & Radojević, 2017).

After drying, the greenware is thermally sintered to obtain the desired ceramic piece. Sintering is the process of compacting and forming a solid mass of material by heat or pressure without melting it to the point of liquefaction. Sintering in practice involves the control of both densification and grain growth. Densification is the act of reducing porosity in a sample thereby making it denser. In the fabrication of porous ceramic materials, the right firing temperature must be selected because excessive heating may lead to vitrification, in which case, the imparted pores necessary for water filtration are filled with glassy materials.

At elevated temperatures, Kaolinite, Talc and vermiculite dehydrate and dehydroxylate transforming into the new crystalline phases (Valášková, 2015). Kaolinite dehydration starts from 20 to 200°C. Dehydroxylation and structural changes occur in three stages (Valášková, 2015):

(i) 450 – 700 °C: Structural change to the metakaolinite (Equation 1)

$$Al_2O_3 \cdot 2SiO_2 \cdot 2H_2O \rightarrow Al_2O_3 \cdot 2SiO_2 + 2H_2O \quad (1)$$

(ii) 930 – 980 °C. Recrystallization of γ-$Al_2O_3$ and metakaolinite to Si-Al spinel.

(iii) 1200 -1250 °C; Crystallization of mullite ($3Al_2O_3$ $2SiO_2$) and cristobalite ($SiO_2$).

Talc begins dehydroxylate at 800 ℃ to the 900 ℃ and transforms to enstatite and cristobalite (Equation 2),

$$Mg_3Si_4O_{10}(OH) \rightarrow 3MgSiO_3 + SiO_2 + H_2O \quad (2)$$

Heating vermiculite at a temperature of 900 °C leads to the transformation of the interlayer water into steam, though the dehydration may start at a temperature below 700 ℃ (Bergaya & Lagaly, 2013). The consequential increase in pressure disruptively separates the silicate layers making the flakes to expand into accordion-like particles (Bergaya & Lagaly, 2013), a phenomenon known as exfoliation. This exfoliation leads to a 10 to 20 times volume increase, significantly lowering the density of the material. The massive thermal expansion of vermiculite during thermal sintering causes cracking of the objects fabricated with clays containing high vermiculite content (Okada *et al.*, 2008), limiting its application in the fabrication of clay ceramic objects. The exfoliated material is rendered chemically inert with excellent thermal and acoustic insulation properties. Some of the common applications of exfoliated vermiculite are the making of thermal insulators, brake linings, friction lightweight aggregates, various construction products (Bergaya & Lagaly, 2013).

## 2.3 Carbonate Minerals and Carbonate Rocks

### 2.3.1 Carbonate Minerals

There exist about sixty minerals containing carbonate ion in their composition. Of these, three stick out of the rest in their abundance and economic importance: calcite, aragonite and dolomite (Bissell & Chilingar, 1967). These carbonates form from mainly calcium ($Ca^{2+}$), magnesium ($Mg^{2+}$) and carbonate ($CO_3^{2-}$) ions. Calcite and aragonite are polymorphous to each other, having the same chemical composition but different crystal structures. Calcite, which forms trigonal crystals, is the most stable polymorph ($CaCO_3$) and the principal constituent of limestone and marble. Aragonite, with orthorhombic symmetry, is a metastable polymorph of $CaCO_3$ and thermodynamically unstable; converting fairly rapidly to calcite under aqueous conditions. Dolomite, on the other hand, is a rhombohedral carbonate consisting of alternating sheets of the cations ($Mg^{2+}$ and $Ca^{2+}$) and the carbonate ions. The formula of ideal (stoichiometric) dolomite is $CaMg(CO_3)_2$. However, due to incomplete dolomitization of the parent limestone, many dolomites do not have the stoichiometric composition. The Mg and Ca content may, therefore, be present in the stoichiometric ratio (as the formula indicates, Ca:Mg = 0.50:0.50) or non-stoichiometric composition ($Ca_{x-y}Mg_y(CO_3)_2$) in alternating layers

separated by $CO_3$ layers (Bissell & Chilingar, 1967). The mineral (dolomite) crystallizes in the trigonal-rhombohedral system. Other sedimentary carbonates of non-negligible importance are magnesite (magnesium carbonate) and siderite (ferrous iron carbonate). The dolomites containing some percentage of $Fe^{2+}$ are called ferroan dolomite.

### 2.3.2 Carbonate Rocks

Carbonate rocks are a class of sedimentary rocks composed primarily of carbonate minerals (Bissell & Chilingar, 1967). The two major types are limestone, which is composed of calcite or aragonite, and dolomite rock, also known as dolostone, which is composed of mineral dolomite ($CaMg(CO_3)_2$). Limestones are those rocks composed of more than 50% carbonate minerals, of which 50 % or more consist of calcite and/or aragonite (Bissell & Chilingar, 1967). Limestones may be white, gray, dark gray, yellowish, greenish, blue and, sometimes, black in color. Dolostones are rocks composed mainly of the mineral dolomite ($CaMg(CO_3)_2$) ≥75%. Rocks that contain 10-50% dolomite mineral are referred to as dolomitic. Impurities in dolomite rock (dolostone) include gypsum, anhydrite, iron sulfides, celestite, opal, chalcedony, iron oxides, magnesite, fluorite and organic matter (Bissell & Chilingar, 1967). Most dolostones are believed to be produced by recrystallization of pre-existing limestones by a process called dolomitization (Sibley & Gregg, 1987). However, the process is often incomplete resulting in carbonate rocks containing a mixture of dolomite ($CaMg(CO_3)_2$), dolomitic-limestone (when $CaCO_3$ in non-stoichiometric dolomite mineral is between 50 and 90%) and limestone ($CaCO_3$) (Sibley & Gregg, 1987). Dolomites are quite similar to limestones in appearance and therefore, it is difficult to distinguish between the two with a naked eye (Sibley & Gregg, 1987). Unmodified carbonate rocks have low aqueous fluoride removal capacity (Cyriac, 2011; Nath & Dutta, 2012). They show improved fluoride removal capacity when amended with acids (Nath & Dutta, 2012).

When calcined at high temperature, the calcite/aragonite ($CaCO_3$) mineral in limestone decomposes into calcium oxide and carbon dioxide (Equation 3). Dolomite ($CaMg(CO_3)_2$), the major mineral in dolostone, on the other hand, decomposes at relatively higher temperature into magnesium oxides, calcium oxide and carbon dioxide (Equation 4).

$$CaCO_3 \xrightarrow{700\ ^\circ C} CaO + CO_2 \quad (3)$$

$$CaMg(CO_3)_2 \xrightarrow{950\ ^\circ C} MgO + CaO + 2CO_2 \quad (4)$$

## 2.4 Calcium Phosphate System and Water De-Fluoridation

Calcium phosphate systems, both natural (bone char) and synthetic, exhibit high de-fluoridation activities. Calcium phosphate compounds such as hydroxylapatite (George, Mehta & Saharan, 2018), octacalcium phosphates (Idini, Dore, Fancello & Frau, 2019), brushite (Mourabet *et al.*, 2011) and amorphous calcium phosphate (Kanazawa, Umegaki & Shiba, 1983) are known to exhibit fluoride adsorption properties (Yakub & Soboyejo, 2013). Since calcium phosphate compounds prepared in aqueous solutions are usually nanomaterials, their removal after adsorption is a challenge due to their small size and health and environmental issues (Ali, 2012).

Calcination/sintering is a solution to this challenge as larger particles are formed. In addition, when these compounds are sintered/calcined, they may be transformed into phases such as calcium pyrophosphate (CPP), tricalcium phosphates, or more crystalline hydroxylapatite (Dosen & Giese, 2011; Karampas & Kontoyannis, 2013; Shiryaev, Safronova & Putlyaev, 2010, Zyman, Goncharenko & Rokhmistrov, 2017). These phases also may have fluoride adsorption properties. Therefore, calcium phosphate system can be incorporated in clay ceramics to impart fluoride adsorption properties.

# CHAPTER THREE

# MATERIALS AND METHODS

## 3.1 Material Collection, Preparation and Synthesis

As discussed in section 2.2, there are many types of clay depending on the clay minerals they contain Kaolin is selected due to being less susceptible to cracking during drying and thermosintering (section 2.2 of this work). On the other hand, carbonate rocks (limestone and dolostone) were used owing to their rich in calcium and magnesium (Section 2.3 of this work).

When calcined at high temperature, the calcite and/or aragonite ($CaCO_3$) mineral (s) in limestone, decomposes into calcium oxide and carbon dioxide (Section, 2.3.2, Equation 3). Dolomite (stoichiometric ($CaMg(CO_3)_2$) or non-stoichiometric ($Ca_{x-y}Mg_y(CO_3)_2$), the major mineral in dolostone, on the other hand, decompose at a relatively higher temperature into magnesium oxides, calcium oxide and carbon dioxide (Section, 2.3.2, Equation 4).

The oxides that result from the calcination react with phosphoric acid to yield calcium phosphates. A multi-phasic calcium phosphate system, containing apatite and non-apatite phases may result (Equation 5). These phases are responsible for fluoride uptake from aqueous solution (Section 2.4)

$$CaO + MgO + H_3PO_4 + H_2O \rightarrow \text{Magnesium/calcium phosphate phases} \qquad (5)$$

This reaction is also expected to occur in the clay matrix (in-situ synthesis of calcium phosphate system).

### 3.1.1 Precursor Material Collection

Three types of carbonate rocks were collected from Merelani Tanzanite mine area (in Manyara region), Kunduchi Beach area (in Dar es Salaam) and Kwamsisi (Korogwe, Tanga), Tanzania. Clay (Kaolin) was collected from Pugu hills (about 20 km south-west of Dar es Salaam), Kisarawe district, in Cost Region, Tanzania. Reagent grade phosphoric acid, originating from Sgma-Aldrich, was purchased at a local store in Arusha.

### 3.1.2 Precursor Material Preparation

The rocks were ground in a ceramic ball mill at The African Minerals and Geosciences Centre in Dar-es-salaam, Tanzania. The powder was sieved with 125 µm sieve and the obtained powder was heat pretreated at 950 ℃ for 8 hours to covert the carbonate minerals in the rocks (calcite or aragonite and dolomite) into oxides of the metal cations they contain.

Figure 2 is a pictorial presentation of the major stages of carbonate rock materials preparation.

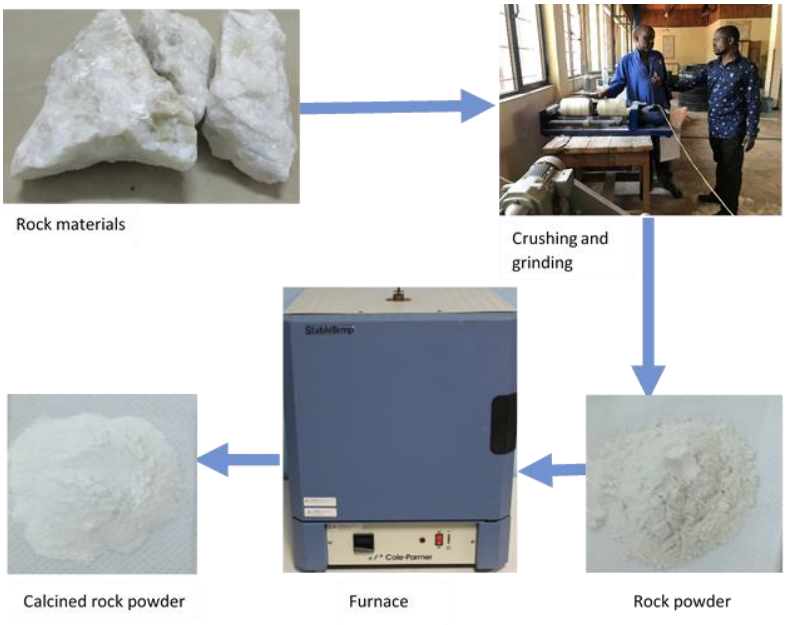


**Figure 2: Carbonate rock preparation; crushing, grinding and heat pretreatment**

### 3.1.3 Synthesis of Ca/Mg Phosphate System and Clay-Mg/Ca Phosphate Composite Ceramic Pellets

Each rock material was used to prepare five different types of adsorbents by varying the proportion of each carbonate rock material clay powder. Clay (K) was added to carbonate rock (R) in different ratios by weight (K:R = 100:0, 90:10, 85:15, 75:25 and 0:100) in beakers at ambient temperature (20 – 26 ℃). Then sawdust, obtained from a local sawmill and sieved through 125 µm sieve was added in a ratio of 2 (clay and dolostone) to 1 (sawdust) by volume to introduce a porous network into the resulting pellet. Then 600 mL of distilled water was added to each beaker and left to soak overnight. The content was then transferred into a laboratory blender to provide vigorous agitation while adding 25% (by weight) phosphoric acid slowly. The amount of phosphoric acid added to 100 g of the mixture was as follows; 0 mL, 21 mL, 32 mL, 52 mL and 52 mL to K:R = 100:0, 90:10, 85:15, 75:25 and 0:100 respectively.

Except for K:R = 100:0, the material thickened with the addition of phosphoric acid. Preliminary studies demonstrated that a dolomite fraction of greater than 25% results in poor sintering and yields a material that exhibits poor mechanical properties, hence susceptible to easy breakage. The initial pH before the addition of phosphoric acid was about 12.1 - 12.5. When pH dropped down to 7.5, the addition of phosphoric acid was stopped for a while until it built up again to above 9.5. The mixture was transferred into plastic beakers and left to age for two days at 45 ℃ in an oven. The matured mixture was dried in an oven at 70 ℃ until it was plastic enough to mold. The resulting plastic material was then molded into discs, by hydroplastic forming method, using a cylindrical mold with internal dimensions of approximately 50 and 10 mm in diameter and depth respectively. The discs were allowed to dry for approximately 2 days after which they were sintered in a furnace at 500, 600, 700, 800 and 900 ℃ for three hours. The ramp rate to peak temperatures was set at 10 °C/min. After sintering, the furnace was then turned off and allowed to cool to room temperature. Figure 3 is a pictorial presentation of the major stages during the synthesis of the materials.

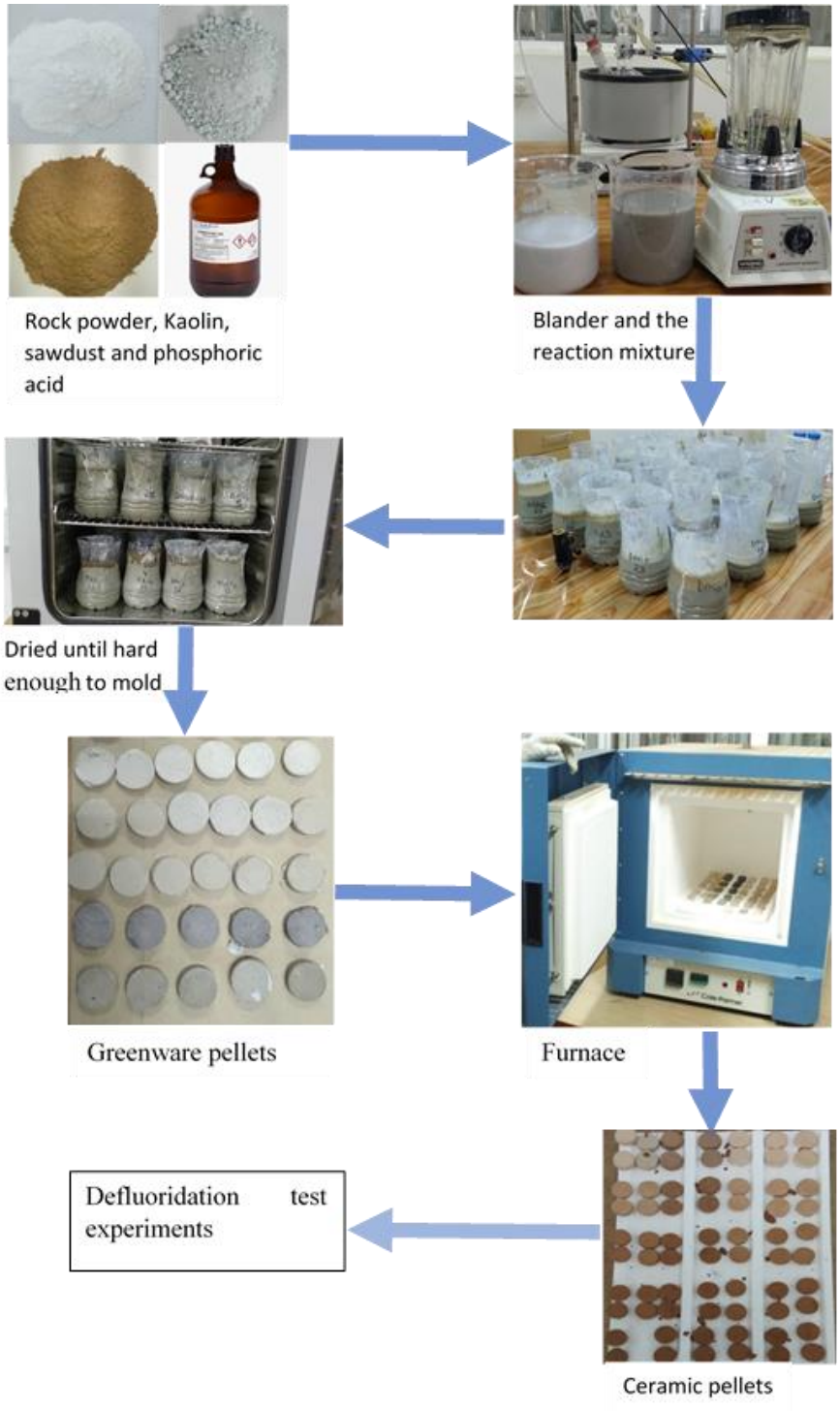


**Figure 3: Ceramic material synthesis main stages**

## 3.2 Material Characterization

### 3.2.1 X-Ray Fluorescence Analysis

Elemental composition analysis of the precursor materials (carbonate rocks and clay) was made using EDXRF X-ray tube excitation Spectrometer (SPECTRO XEPOS). The EDXRF excite the sample with three Targets namely Mo-Secondary target (45kV), $Al_2O_3$ polarization target (49.5 kV) and HOPG Bragg Crystals (25kV) for sixteen minutes. Samples were measured in triplicate. Soil Montana was used as the standard reference material.

### 3.2.2 CHNS-O Analyzer

The carbon content of the carbonate rock materials was determined using CHNS-O analyzer; Thermo Scientific™ FLASH 2000 CHNS/O. The samples were crushed and homogenized using a mortar and pestle and weighed into tin sample cups with vanadium pentoxide catalyst. Six point calibration of the instrument using 2.5-Bis(5-tert-butyl-benzoxazol-2-yl)thiophene (BBOT) was conducted before experimenting. The calibration verification standard, (Quality Control check standard, BBOT), was run with the batch.

### 3.2.3 Atomic Absorption Spectrometer

Shimadzu AA-6200 atomic absorption spectrophotometer (AAS) was used to quantify Calcium and Magnesium in rock samples. Sample of weight 1g of ground material was digested with hydrochloric acid according to (Robinson, 1980). The resultant solution was diluted to make one liter with distilled water and used to quantify calcium and Magnesium.

### 3.2.4 Fourier-Transform Infrared Spectroscopy

Fourier-transform infrared spectroscopy (FTIR) using BRUKER ALPHA spectrometer was used for the identification of carbonate minerals in rocks and chemical characterization of the phosphate system. Tests were conducted in absorbance mode in spectral range of 4000 – 400 $cm^{-1}$ with a resolution of 2 $cm^{-1}$.

### 3.2.5 Atomic Pair Distribution Function Analysis

The atomic pair distribution function (PDF) technique was used to study phase composition and crystallite size of both the synthesized material and some of precursor materials (Billinge, 2019). The PDF experiments were carried out at the XPD beamline at NSLS-II at Brookhaven

National Laboratory using the rapid acquisition PDF method (RAPDF)1. A 2D Perkin Elmer amorphous silicon detector was placed 206 mm behind the samples, which were loaded in 1 mm ID kapton capillaries. The incident wavelength of the x-rays was 0.1949 λ. Calibration of the experimental setup was done using Nickel as a calibrant. Data sets were collected at room temperature. Raw data were summed and corrected for polarization effects before being integrated along arcs of constant angle to produce 1D powder diffraction patterns using the program pyFAI[2]. Corrections were then made to the data and normalization are carried out to obtain the total scattering structure function, F(Q), which was Fourier transformed to obtain the PDF using PDFgetX3[3] within xPDFsuite[4]. The maximum range of data used in the Fourier transform was $Q_{max}$ = 22 $Å^{-1}$. The modeling is carried out using Diffpy-CMI[5].

### 3.2.6 Thermogravimetric Analysis

Thermogravimetric analysis (TGA) was conducted to study the physical and chemical properties of the synthesized materials as a function of increasing temperature. Thermogravimetric analysis (TGA) of the prepared materials was performed using QT-STA-100 Tester instrument at a heating rate of 10 °C $min^{-1}$ from room temperature 25 °C to 900 °C.

### 3.2.7 Water Physical Parameters

Multiparameter water quality Meter (Hanna® 9829) was used to measure the physical parameters of water.

### 3.2.8 Selected Chemical Parameters of Water

Phosphate concentration was determined calorimetrically using DR 2800 spectrophotometer-ach and PhosVer® 3 Phosphate Reagent powder pillow. Calcium and Magnesium were determined by EDTA titrations.

## 3.3 De-Fluoridation Experiments

### 3.3.1 Water Sample, Equipment and Reagent

De-fluoridation experiments were conducted using simulated water and natural water. Simulated water (1000 mg/L) was prepared by dissolving 2.100 g of NaF in 1 L of distilled water. Dilution was made to obtain 50 m g/L and 10 mg/L of $F^-$. Natural water was obtained from Uluwile river and Belem spring. Quantification of $F^-$ concentration was achieved using

ion-selective electrode (ISE) connected to a Mettler Toledo seven compact pH/IonS220 m (Fig. 4Figure 4). The ISE was dipped in a mixture of equal volumes of fluoride water and total ionic strength buffer (TISAB II) (ratio of 1:1) for 10 s before taking measurements. The calibration of the instrument was conducted according to the manufacturer's user manuals.

### 3.3.2 Ceramic Pellets

To assess the de-fluoridation performance of the ceramic adsorbent pellets prepared using carbonate materials collected from Kunduchi (Calcite), Tanga (Kwamsisi) (near-stochiometric dolomite) and Merelani (magnesium deficient dolomite) and determine their potentiality as sources of cations, de-fluoridation efficiency was determined. A pellet weighing 2.0 g and sintered at 700 ℃ was put in 250 mL conical flask containing 50 mL of 10 mg/L fluoride. After 12 hours, the final fluoride concentration ($C_t$) was measured. The experiment was carried out at ambient temperature (24 - 28 ℃) without shaking. De-fluoridation efficiency (%E) was then calculated using equation 6.

$$\%E = \left(\frac{C_o - C_t}{C_o}\right)100 \qquad (6)$$

Where %E is the de-fluoridation efficiency, $C_o$ is the initial fluoride concentration and $C_t$ if the final fluoride concentration.

### 3.3.3 Ground Ceramic Materials

Experiments to determine the variation of de-fluoridation amount (amount of fluoride removed per unit mass of adsorbent, mg/g) with adsorbent doses were conducted using ground material of mass between 0.0100 g and 0.300 g. in 50 mL of water with specified $F^-$ concentration (10 mg/L, 12.4 mg/L, 48 mg/L and 50 mg/L). A mixture of weighed material and 50 mL of 10 mg/L $F^-$ simulated water (or natural water) were shaken in falcon tubes (horizontally positioned) on Retch AS 200 shaker with an amplitude of 70 for 6 hours (at equilibrium). The concentration of fluoride at equilibrium ($C_e$, mg/L) was measured along with the final pH.

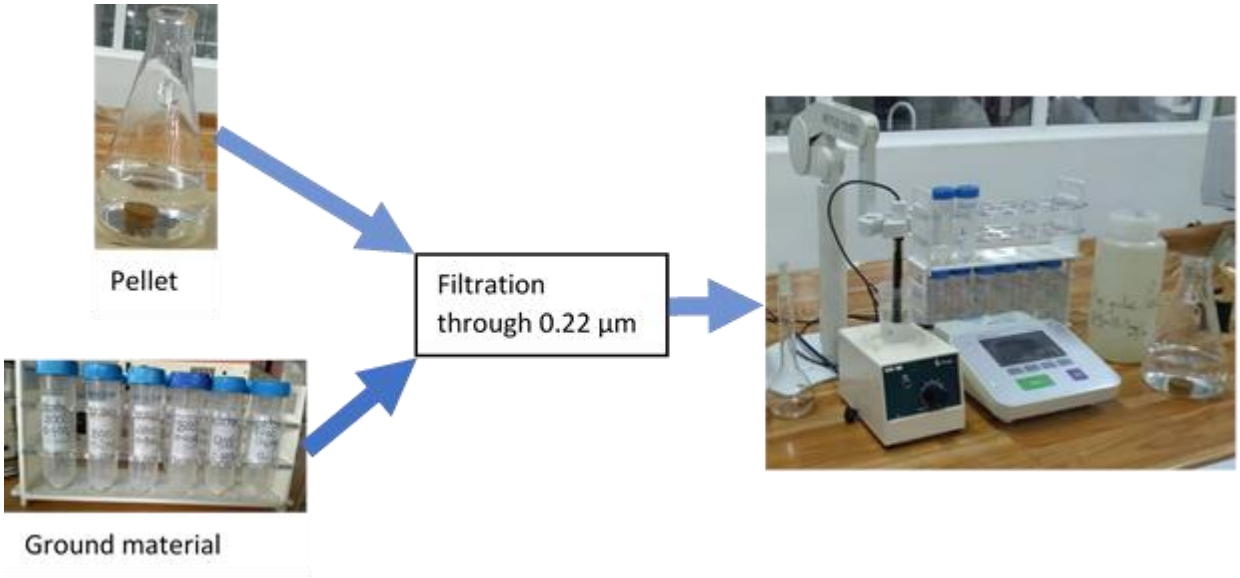


**Figure 4: Adsorption fluoride test**

The data were used to determine the de-fluoridation amount ($q_e$, mg/g), was calculated using equation 7.

$$q_e = \frac{(C_0 - C_e)}{m} V \qquad (7)$$

where $q_e$ is the de-fluoridation amount (defined as mass of $F^-$ adsorbed per unit mass of adsorbent material) ($q_e$, mg/g), $C_o$ is the initial $F^-$ concentration (mg/L), $C_e$ is the $F^-$ concentration at equilibrium (mg/L), V is Volume (L) and m is mass of adsorbent (g).

### 3.3.4 Kinetic Experiments

For kinetics, a series of 0.1 g of ground adsorbent materials in 50 mL were prepared and allowed to adsorb in 250 mL conical flasks at pre-determined time intervals. The process was brought at a halt by filtering off the adsorbent with a vacuum filtration unit mounted with 0.22 µm filter paper. The $F^-$ concentration (mg/L) at time t (min) ($C_e$) was measured and used to calculate the de-fluoridation amount at time t (h) using equation 8.

$$q_t = \frac{(C_0 - C_t)}{m} V \qquad (8)$$

where $q_t$ is $F^-$ adsorbed at time t (mg/g), $C_o$ is the initial $F^-$ concentration (mg/L), $C_t$ is $F^-$ concentration at time t (mg/L), V is volume (L) and m is mass of adsorbent (g).

## 3.4 Adsorption Isothermal Models

Adsorption isothermal models were used to evaluate the theoretical de-fluoridation capacity ($Q_m$) and to gain insight into the fluoride removal mechanism. Two adsorption isothermal models, Langmuir and Freundlich, were used in this work.

### 3.4.1 Langmuir Isotherm Model

It is a model that is based on the assumption that adsorption occurs on a homogeneous surface through the same mechanism, forming a monolayer deposit of adsorbate molecules/species (Liu, 2015). In this model, the adsorption sites are assumed to be equivalent, with equal energy, and equally available. The adsorbing species are assumed to be points (point sized), therefore there is no interaction with the adsorbed species (Liu, 2015). Since active sites are equal in terms of energy, the interactions between adsorbate molecules and the adsorbent are also assumed to be uniform.

$$\frac{C_e}{q_e} = \frac{1}{K_L Q_m} + \frac{1}{Q_m} C_e \qquad (9)$$

where $Q_m$ is the maximum adsorption capacity (mg/g), and $K_L$ is the Langmuir constant (g/L) related to the free energy of adsorption. A linear plot of $C_e/q_e$ versus $C_e$ giving correlation coefficients ($R^2$) close to unity validates Langmuir. Values of $Q_m$ and $K_L$ are obtained from the slope and the intercept of $C_e/q_e$ versus $C_e$ plot respectively. It is known that in some cases Langmuir model proves inadequate in describing some adsorbate-adsorbent systems that would be expected to form a monolayer deposit. Adsorption that deviates from the adsorption isotherm of the Langmuir model is termed as cooperative adsorption. The deviation is caused by interactions among adsorbates or non-uniform interactions between the adsorbate and the adsorbent.

### 3.4.2 Freundlich Adsorption Isotherm

This is an empirical equation (Equation 10 and 11) that describes the adsorption characteristics of an adsorbent onto a heterogeneous adsorbent surface. Unlike Langmuir Isotherm, the model accommodates the formation of a multi-layered deposit onto the adsorbent and allows energy level differences among the adsorption sites of the adsorbent (Desta, 2013; Liu, 2015).

$$q_e = K_f C_e^{1/n} \qquad (10)$$

A linearized equation is;

$$\ln q_e = \ln K_f + 1/n \ln C_e \quad (11)$$

Where $K_f$ is Freundlich isotherm constant (mg/g), n is adsorption intensity; $C_e$ is the equilibrium concentration of adsorbate (mg/L) $q_e$ is the amount of adsorbate adsorbed per gram of the adsorbent at equilibrium (mg/g).

### 3.5 Kinetics Models

To understand the adsorption kinetics of adsorbents and gain insight of the adsorption mechanism (including potential rate-controlling steps), four kinetic models will be used; the pseudo-first-order model (Rodrigues & Silva, 2016; Simonin, 2016), pseudo-second-order model (Gosset, Trancart & Thévenot, 1986; Ho, 1995), particle diffusion model and the intraparticle diffusion model (Haerifar & Azizian, 2013; Liu, 2015; Weber & Morris, 1963) (Table 1). The first two models (pseudo-first-order and pseudo-second-order model) are chemical rate laws while the later (particle diffusion and intra-particle diffusion model) hold for diffusion-controlled sorption processes (Gosset *et al.*, 1986; Liu, 2015).

**Table 1: Kinetic models**

| Model | Linearized equation | Parameters |
|---|---|---|
| Particle diffusion model | $\ln(1-\alpha) = -k_p t$ | $\alpha$ is the fractional attainment of equilibrium, $q_t$ is the quantity of adsorbed fluoride per gram of adsorbent material at any given time (mg/g) $k_p$ is the particle rate constant ($min^{-1}$) |
| Intraparticle diffusion model | $q_e = k_d t^{1/2}$ | $k_d$ is the intra-particle diffusion rate constant ($mg/g \cdot min^{1/2}$) |
| Pseudo-First-Order Kinetic Model | $\log(q_e - q_t) = \log q_e - (k_1/2.303)t$ | $q_e$ is the quantity of adsorbed fluoride per gram of adsorbent material at equilibrium (mg/g). $K_1$ is the rate constant for pseudo 1st order ($min^{-1}$) |
| Pseudo-Second-Order Kinetic Model | $t/q_t = 1/K_s(q_e)^2 + t/q_e$ | Ks is the rate constant for pseudo 2nd order (g/(mg min) |

# CHAPTER FOUR

# RESULTS AND DISCUSSION

## 4.1 Precursor Material Characterization

### 4.1.1 XRF, AAS and CHNS-O Analyzer

Table 2 presents XRF elemental analysis of the carbonate rock materials collected from Kunduchi (in Dar es salaam), Kwamsisi (Tanga), and Marelani (Manyara) respectively. The results show that the rock materials collected from Kunduchi are composed of calcium as the main cation (a metallic element). On the other hand, the carbonate rocks obtained from Kwamsisi (in Tanga) and Merelani (in Manyara region) are composed of calcium and magnesium as the main cations. The AAS results indicated that calcium and magnesium content of the rocks materials were (243 ± 2) mg/g and (112 ± 1) mg/g for the Merelani rock materials and (243 ± 2) mg/g and (134 ± 1) mg/g for the Kwamsisi (Tanga) materials. CHNS/O Analyzer showed that the carbon content of the carbonate rocks are; (13.8 ± 0.6)%, (13.4 ± 0.6)%, and (11.5 ± 1)%, for Merelani, Tanga (Kwamsisi) and Kunduchi materials respectively. The calcium and carbon the content ((37.5 ± 0.1)% and 11.5 ± 1)%) of the Kunduchi materials are close to the stoichiometric composition of pure $CaCO_3$ (40%, 12%). The lower carbon and calcium content of this material (from Kunduchi) than the stoichiometric composition of the $CaCO_3$ is due to the presence of silica/quartz and other minor impurities as shown by XRF results. This shows that the material is composed of mainly calcite or aragonite minerals, evidencing that the rock materials collected from Kunduchi are limestone. For the Merelani and Tanga materials, the calcium and magnesium content (24.17% and 10.82% for Merelani, and 24.92% and 11.78% for Tanga carbonate) considered together with carbon content suggest that the rocks could be dolostone (composed of either stoichiometric or non-stoichiometric dolomite), dolomitic limestone or a complex mixture including magnesite. Stoichiometric dolomite contains 21.7% and 13.04% of calcium and magnesium respectively. Table 3 shows the elemental composition of Pugu clay (kaolin).

**Table 2: Percentage elemental composition of rock materials collected from Kunduchi (in Dar-es-Salaam), Kwamsisi (in Tanga) and Merelani (in Manyara)**

| N | Symbol | Name | Kunduchi | | Merelani | | Merelani | |
|---|---|---|---|---|---|---|---|---|
| | | | Average % | Standard deviation | Average % | Standard deviation | Average % | Standard deviation |
| | L.O.I. | Loss on Ignition | 56.73 | 0.060 | 62.22 | 0.200 | 64.49 | 0.10 |
| 11 | Na | Sodium | 0.004 | 0.007 | 0.00 | 0.00 | 0.00 | 0.00 |
| 12 | Mg | Magnesium | 0.157 | 0.010 | 11.78 | 0.10 | 10.82 | 0.08 |
| 13 | Al | Aluminum | 1.752 | 0.011 | 0.00 | 0.00 | 0.00 | 0.00 |
| 14 | Si | Silicon | 3.133 | 0.023 | 0.94 | 0.01 | 0.40 | 0.001 |
| 17 | Cl | Chlorine | 0.014 | 0.000 | 0.07 | 0.003 | 0.011 | 0.02 |
| 19 | K | Potassium | 0.076 | 0.007 | 0.00 | 0.00 | 0.00 | 0.00 |
| 20 | Ca | Calcium | 37.52 | 0.043 | 24.92 | 0.08 | 24.17 | 0.07 |
| 22 | Ti | Titanium | 0.05 | 0.001 | 0.00 | 0.00 | 0.00 | 0.00 |
| 25 | Mn | Manganese | 0.033 | 0.001 | 0.01 | 0.004 | 0.003 | 0.0001 |
| 26 | Fe | Iron | 0.461 | 0.003 | 0.43 | 0.02 | 0.34 | 0.002 |
| 38 | Sr | Strontium | 0.034 | 0 | 0.08 | 0.006 | 0.022 | 0.003 |
| 56 | Ba | Barium | 0.011 | 0.003 | 0.04 | 0.002 | 0.021 | 0.003 |

**Table 3: Percentage elemental composition of Pugu Kaolin**

| N | Symbol | Name | Average % | Standard deviation |
|---|---|---|---|---|
| | L.O.I. | Loss on Ignition | 61.17 | 0.250 |
| 11 | Na | Sodium | 0.40 | 0.013 |
| 12 | Mg | Magnesium | 1.16 | 0.009 |
| 13 | Al | Aluminum | 7.55 | 0.054 |
| 14 | Si | Silicon | 24.43 | 0.149 |
| 15 | P | Phosphorus | 0.02 | 0.001 |
| 16 | S | Sulfur | 0.01 | 0.002 |
| 17 | Cl | Chlorine | 0.18 | 0.009 |
| 19 | K | Potassium | 1.02 | 0.005 |
| 20 | Ca | Calcium | 0.33 | 0.001 |
| 22 | It | Titanium | 0.34 | 0.001 |
| 24 | Cr | Chromium | 0.02 | 0.001 |
| 25 | Mn | Manganese | 0.01 | 0.000 |
| 26 | Fe | Iron | 3.00 | 0.026 |
| 56 | Ba | Barium | 0.24 | 0.010 |

### 4.1.2 Mineral Identification of the Carbonate Rocks by Fourier-Transform Infrared Spectroscopy

Different minerals with the same chemical composition may exhibit different reactivities, thereby affecting the quality and performance of the final product for the intended application. It is for this reason that efforts were made to identify the minerals present in carbonate materials. in this study Fourier-Transform Infrared Spectroscopy (FTIR) was used for identification of the major minerals present in the rock materials.

The three rock materials used in this study exhibit FTIR peaks typical of carbonate materials containing some quartz or silica impurities. The carbonate ion bands are shown in Table 4. For the Kunduchi materials, the peak at 470 $cm^{-1}$ assignable to Si-O (symmetrical stretching Si-O) (Sağın, Böke, Aras & Yalçın, 2012; Sdiri, Higashi, Hatta, Jamoussi, & Tase, 2010) is distinct. The Kunduchi and the Merelani materials showed a broad band in the low frequency range at around 1200 – 900 $cm^{-1}$, ascribable to Si-O and Si-O-Si vibrations, suggesting the presence of quartz (Sağın *et al.*, 2012; Sdiri *et al.*, 2010). The intensity of the broad band (1200 – 900 $cm^{-1}$) was lower in the Merelani materials, signifying lower level of silica/quartz. Figure 8 presents superimposed spectra of the three rock materials. It can be seen from Figure 8 that the intensity of the peaks assignable to quartz decreases in the order; Kunduchi > Tanga > Merelani. This is consistent with the XRF results which show decrease in silicon content of the material in the same order; Kunduchi (3.1%) > Tanga (0.94) > Merelani (0.40%) (Table 2).

Several researchers have studied and employed FTIR analysis as a rapid technique for identifying dolomite (Boggs & Boggs, 2009; Jovanovski, Stefov, Šoptrajanov, & Boev, 2002; Stanienda-Pilecki, 2019). In this study, FTIR peak position was used to identify the carbonate rock materials used. Figure 5-7 present individual spectra of the carbonate rock materials used in this study. The principle behind this carbonate mineral identification technique is that peaks shift from their respective positions as a result of a change in the chemical environment of the carbonate ion. Variations in the $CO_3^{2-}$ peak locations on the FTIR spectrum shows differences in the chemical environment of the ion. The $CO_3^{2-}$ ion chemical environment due to neighboring atom in the lattice crystal structure varies with the carbonate mineral type, leading to a shift in its peak position on the FTIR spectrum (Pokrovsky, Mielczarski, Barres, & Schott, 2000; Stanienda-Pilecki, 2019).

Table 4 presents selected $CO_3^{2-}$ FTIR peaks/bands extracted from the spectra of the materials. on the other hand, Table 5 presents FTIR bands/peaks characteristic of carbonate minerals reported in the literature (Boggs & Boggs, 2009; Stanienda-Pilecki, 2019). Literature establishes that free $CO_3^{2-}$ ions exhibit four intra-molecular vibrations: $\nu_1$ (symmetrical stretching), $\nu_2$ (bending beyond the plane), $\nu_3$ (symmetrical stretching), and $\nu_4$ (bending in the plane) (Boggs & Boggs, 2009; Pokrovsky *et al.*, 2000; Stanienda-Pilecki, 2019). When the ion ($CO_3^{2-}$) is in the crystalline lattice of trigonal anhydrous carbonate minerals, vibrations of the $CO_3^{2-}$ anion gives absorption bands slightly shifted compared to the free ion vibrations. Of the bands ($\nu_1$-$\nu_4$), the band $\nu_4$ proves to be particularly useful for the identification of carbonate minerals (Stanienda-Pilecki, 2019). This is because the shift of this band, as the cation changes, is clearer and more pronounced (Stanienda-Pilecki, 2019).

The carbonate minerals were identified on the bases of $\nu_1 + \nu_4$ and $\nu_4$ bands. As expected, the $\nu_4$ band, and to some extent, $\nu_1 + \nu_4$ band, clearly shifted to higher wavenumber values with an increase in magnesium content; Tanga > Merelani > Kunduchi (Table 4) (see XRF results in Table 2 for Mg content). The wavenumber values were very close to the calcite diagnostic values (compare Tables 4 and 5). For the Tanga rocks, the $\nu_1 + \nu_4$ and $\nu_4$ bands were observed at 1817 $cm^{-1}$ and 726.3 $cm^{-1}$, which falls within the range of peaks for dolomite mineral as presented in Table 5 (1815 – 1821 $cm^{-1}$ and 727 – 731 $cm^{-1}$), though $\nu_4$ is 0.7 $cm^{-1}$ below the lower limit. This suggests that the rock materials collected from Tanga are dominated by dolomite mineral, possibly near-stoichiometric dolomite as indicated by being 0.7 $cm^{-1}$ short of stoichiometric dolomite. On the other hand, the $\nu_1 + \nu_4$ and $\nu_4$ bands for the $CO_3^{2-}$ ion of the Merelani rocks features at 1798 $cm^{-1}$ and 715 $cm^{-1}$ respectively. These values are close to the literature values for high Mg-calcite (non-stoichiometric dolomite) Table 5. Based on the literature peak assignments provided in Table 5, there was no band/peak assignable to huntite and Magnesite that featured in the spectra.

**Table 4: Selected Fourier-transform infrared spectroscopy bands for carbonate rocks studied**

| Observed band positions ($cm^{-1}$) of $CO_3^{2--}$ | | | Assignments |
|---|---|---|---|
| **Kunduchi** | **Merelani** | **Tanga** | |
| 709.7 | 715 | 726.3 | $\nu_4$ |
| 871.2 | 854 | 876.8 | $\nu_2$ |
| 1090 | 1090 | 1090 | $\nu_1$ |
| 1400.4 | 1406.6 | 1423.6 | $\nu_3$ |
| 1796 | 1798 | 1817 | $\nu_1 + \nu_4$ |
| 2512 | 2517-2531 | 2531 | $\nu_1 + \nu_3$ |

**Table 5: Fourier-transform infrared spectroscopy characteristic bands ($cm^{-1}$) for carbonate minerals reported in the literature**

| **Calcite $CaCO_3$** | **High Mg-calcite $(Ca_{1-n}Mg_n)CO_3$** | **Dolomite $CaMg(CO_3)_2$** | **Magnesite $MgCO_3$** | **Huntite $CaMg_3[CO_3]_4$** |
|---|---|---|---|---|
| $\nu_4 = 712$ | $\nu_4 = 719$ | $\nu_4 = 727 - 731$ | $\nu_4 = 747-748$ | $\nu_4 = 742-744$ |
| $\nu_2 = 847$ | $\nu_2 = 850$ | $\nu_2 = 852 - 854$ | $\nu_2 = 855$ | $\nu_2 = 846-877$ |
| $\nu_2 = 873-875$ | $\nu_2 = 876$ | $\nu_2 = 878 - 883$ | $\nu_2 = 884-885$ | $\nu_2 = 869-890$ |
| $\nu_1 = 1087$ | $\nu_1 = 1084 - 1088$ | $\nu_1 = 1092 - 1100$ | $\nu_1 = 1108-1113$ | $\nu_1 = 1110-1113$ |
| $\nu_3 = 1409 -1415$ | $\nu_3 = 1426 - 1437$ | $\nu_3 = 1431 - 1451$ | $\nu_3 = 1448 -1456$ | $\nu_3 = 1530$ |
| $\nu_1 + \nu_4 = 1797-1799$ | $\nu_1 + \nu_4 = 1800$ | $\nu_1 + \nu_4 = 1815-1821$ | $\nu_1 + \nu_4 = 1827-1831$ | $\nu_1 + \nu_4 = 1825-1828$ |
| $\nu_1 + \nu_3 = 2512-1519$ | $\nu_1 + \nu_3 = 2517-1519$ | $\nu_1 + \nu_3 = 2525-2538$ | $\nu_1 + \nu_3 = 2535-1537$ | $\nu_1 + \nu_3 = 2581-1583$ |

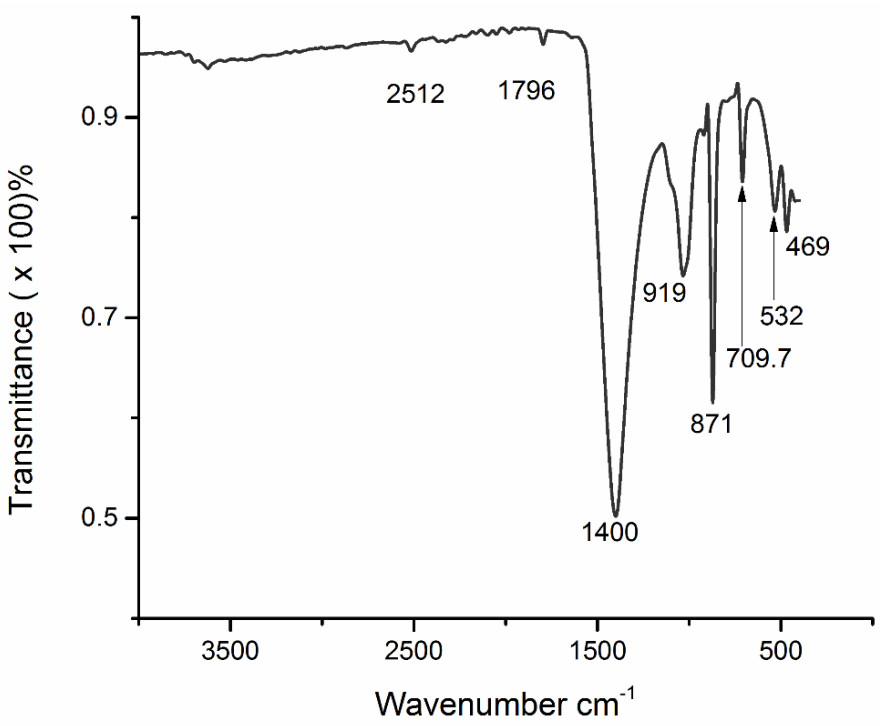


**Figure 5: Fourier-transform infrared spectroscopy (FTIR) spectrum of carbonate materials collected from Kunduchi (in Dar es Salaam)**

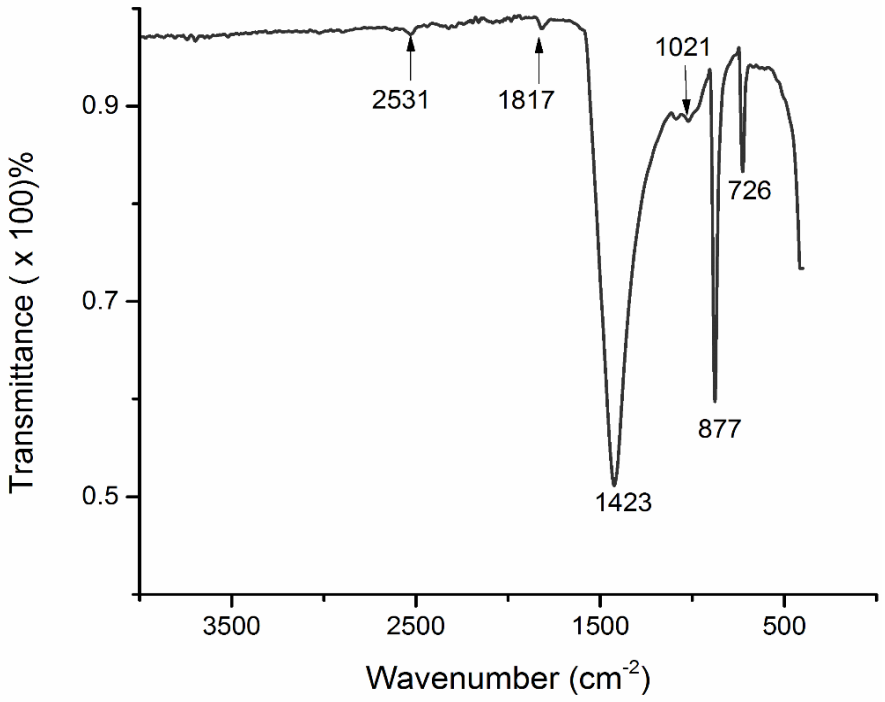


**Figure 6: Fourier-transform infrared spectroscopy (FTIR) spectrum of carbonate rock materials obtained from Tanga (Kwamsisi)**

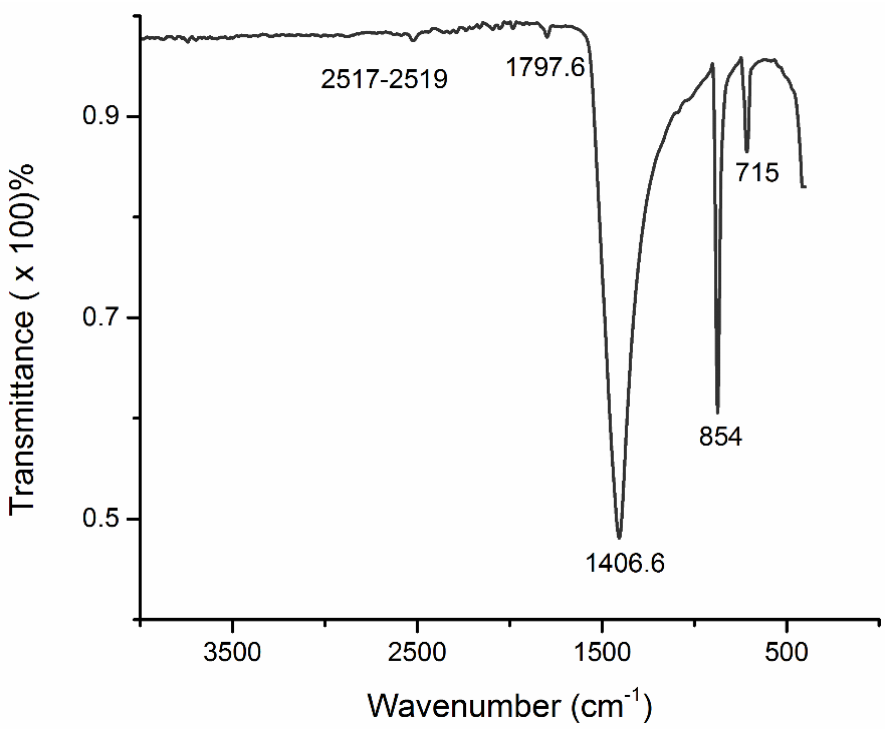


**Figure 7: Fourier-transform infrared spectroscopy (FTIR) spectrum of carbonate rocks collected from Merelani**

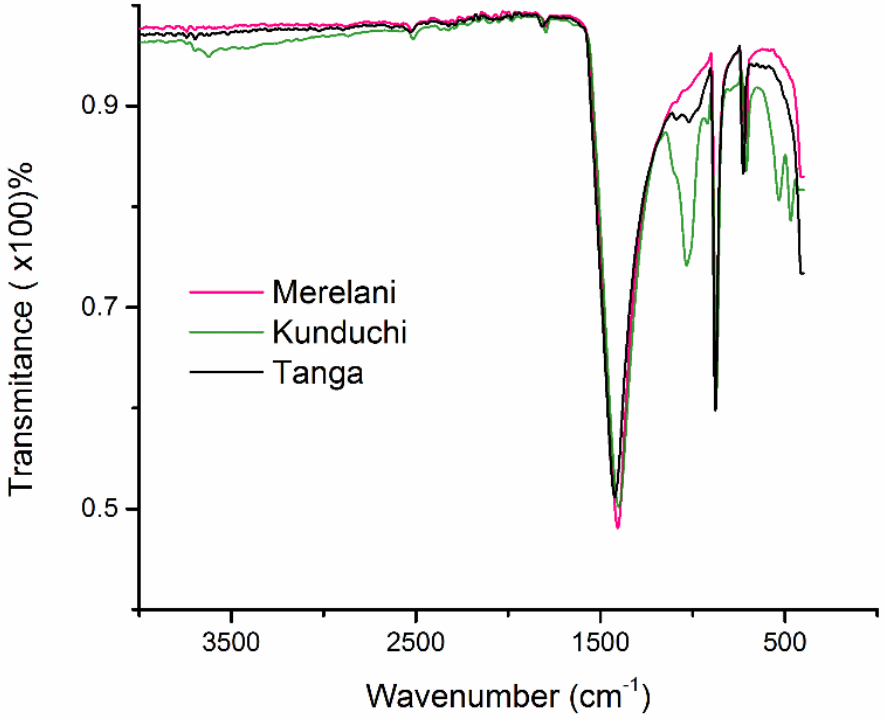


**Figure 8: Fourier-transform infrared spectroscopy (FTIR) spectra of the materials collected from Kunduchi, Kwamsisi and Merelani on one plane**

### 4.1.3 Carbonate Mineral Identification for the Rocks Collected from Merelani by Atomic Pair Distribution Function Analysis

The mineral identification of the rock materials collected from Merelani was confirmed by crystallographic information obtained by the "atomic pair distribution function (PDF) technique". The relatively higher de-fluoridation performance of the adsorbent synthesized using the rock motivated the confirmation. The PDF of the precursor was fitted with a single phase and two-phase models, respectively. Figure 9 presents the PDF of the materials collected from Merelani fitted with the models of dolomite, a mixture of dolomite and calcite, and a mixture of dolomite and magnesite, respectively. In the figure, the circle curves are the measured data, the overlapping solid lines are the calculated PDF from the best fit and the curves below are the residuals. The $R_w$ is the residual factor (reliability factor) (The lower the $R_w$ value the better the fitting). As Fig. 9 presents, the dolomite single phase model shows a good fit with low residual factor value ($R_w$) of 0.274. The low $R_w$ value shows good agreement between the model and the experimental data, and that dolomite contributes the majority of the PDF signals. The two-phase fit involving calcite (dolomite, calcite) produces a small but significant decrease in the $R_w$ (agreement factor) of 0.02, indicating that there is a minority of calcite in the material.

There is no indication of a magnesite signal in the PDF. This implies that most of the magnesium present in the material are part of the dolomite crystal structure. The obtained crystallographic information, including unit cell parameters, presented in Table 6, correspond to dolomite and calcite, where; D is the particle size, a, b and c are lattice parameters, $U_{iso}$ indicates isotropic atomic displacement parameters (ADPs) and δ2 is a fitting parameter that accounts for correlate motion in the PDF. The carbonate rock, as suggested by FTIR, is confirmed to be composed of dolomite mixed with a small amount of calcite and minor impurities. Also as indicated by XRF and FTIR small amount of quartz is present.

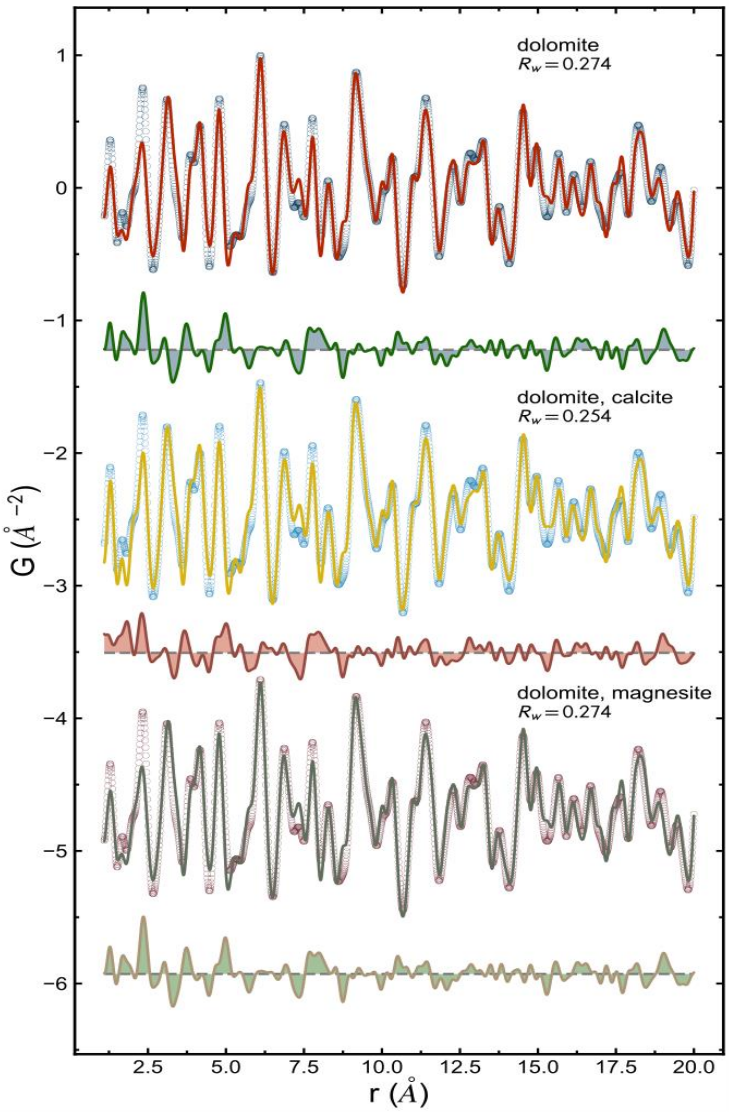


**Figure 9: Atomic pair distribution function (PDF) of rock materials fitted with the models of dolomite, a mixture of dolomite and calcite, and a mixture of dolomite and magnesite respectively. The circle curves are the measured data, the overlapping solid lines are the calculated PDF from the best fit and the curves below are the residuals. The Rw is the residual factor (reliability factor)**

**Table 6: The atomic pair distribution function (PDF) fitting results of the Merelani carbonate rock materials**

| Parameter | Value | |
|---|---|---|
| | Dolomite phase | Calcite phase |
| D (Å) | 88.462 | 82.22 |
| Scale | 0.156 | 0.029 |
| $\delta_2$ (Å$^2$) | 1.54 | 5.082 |
| A | 4.806 | 5.03 |
| B | | 7.583 |
| C | 16.013 | 5.562 |
| $U_{iso}$(Ca)(Å$^2$) | 0.004 | 0.059 |
| $U_{iso}$(Mg)(Å$^2$) | 0.006 | |
| $U_{iso}$(C)(Å$^2$) | 0.005 | 0.641 |
| $U_{iso}$(O)(Å$^2$) | 0.008 | 0.006 |

### 4.1.4 Characterization of the as-Mined Pugu Clay by Fourier-Transform Infrared Spectroscopy

Figure 10 presents Fourier-transform infrared spectroscopy (FTIR) spectra of raw clay (as mined). The vibrations occurring at 3698 cm$^{-1}$ is ascribed to the in-phase OH stretching of the inner surface hydroxyl of the kaolinite (Larbi, Hamou, Bendraoua & Ramdani, 2015). Previous work that characterized beneficiated kaolin observed this band at 3683 cm$^{-1}$ (Dawley, Scott, Hill, Leszczynski & Orlando, 2012; Olejnik, Aylmore, Posner & Quirk, 1968; Sempeho *et al.*, 2015). Vibrations ought to be observed at 3650 cm$^{-1}$ which is due to the out-phase OH stretching vibrations of the inner surface hydroxyl groups was not observed. The band exhibited at 3622 cm$^{-1}$ corresponds to the inner layer OH stretching of AlO-H in the octahedral configuration of kaolinite mineral. Using Beneficiated Pugu kaolin. Sempeho *et al.* (2015) observed this band at 3618 cm$^{-1}$. Another diagnostic OH$^-$ stretching vibrations of the kaolinite in a tetrahedral configuration which should have featured at 749 cm$^{-1}$ (Olejnik *et al.*, 1968; Sempeho *et al.*, 2015) could be overlapping with peaks of other constituents of kaolin in the shoulder between 753 – 769 cm$^{-1}$. The band/shoulder at 1109 -1112 cm$^{-1}$ is assigned to the apical Si-O stretching mode (normal to the planar stretching), this agrees well with the band frequencies of 1113 cm$^{-1}$ reported by (Sempeho *et al.*, 2015). The band at 995 cm$^{-1}$ represents the out-phase Si-O planar stretching (Heah *et al.*, 2012); this is in agreement with the 997 cm$^{-1}$ obtained by (Aroke and El-Nafaty, 2014; Dang, Chen & Lee,

2013; Mgbemena, Ibekwe, Sukumar & Menon, 2013). Owing to presumably bond broadening, the band for in-phase Si-O planar stretching supposed to appear at 1023 $cm^{-1}$ was not observed. The spectrum also features another band at 913 $cm^{-1}$ that is attributed to the $OH^-$ deformation of inner hydroxyl groups due to the Al-OH bending. This falls within the range of frequencies due to the group reported in the literature such as 913 $cm^{-1}$ (Dawley *et al.*, 2012), 907 $cm^{-1}$ (Heah *et al.*, 2012), 912 $cm^{-1}$. The band at 786 $cm^{-1}$ is ascribed to the Al-O-Si asymmetric bending of the bonds whereas the bands at 525 $cm^{-1}$ correspond to the SiO-Al (VI) where $Al^{3+}$ is in octahedral coordination (Heah *et al.*, 2012). On comparison, beneficiated Pugu Kaolin as reported by (Sempeho *et al.*, 2015) gives better resolved FTIR peaks than the un-beneficiated material which was FTIR characterized as mined. Despite band broadening and overlapping leading to obscuring some peaks, major kaolinite diagnostic peaks could still be identified. Based on these FTIR results, supplemented by the work of Sempeho *et al.* (2015), it is evident that the clay material used in this study is indeed Kaolin containing significant amount silica, iron and magnesium compounds (as shown by XRF elemental analysis).

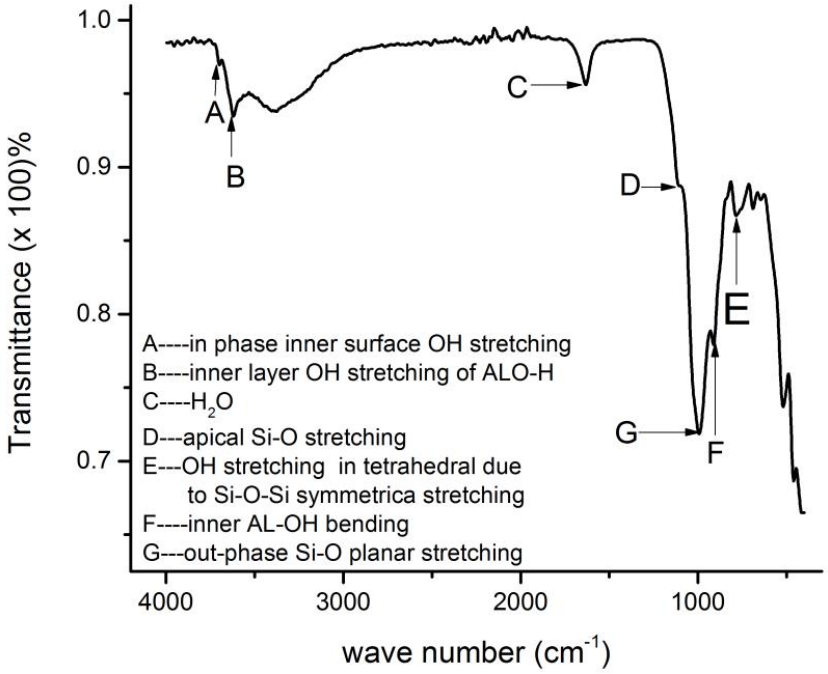


**Figure 10: Fourier-transform infrared spectroscopy (FTIR) spectrum of the as-mined Pugu Kaolin**

### 4.1.5 Summary of the Characterization Results of the Precursor Materials

As evidenced by the calculations made using the data obtained by instrumental analysis (XRF, CHNSO elemental analyzer and AAS), the materials used in this study are carbonate materials

with minor secondary minerals. Based on the results, it was found that the materials sourced from Kunduchi (in Dar es salaam) were high-calcium limestone (calcite/Aragonite). It contained calcium as the dominant cation and carbon content was close to the stoichiometric content of $CaCO_3$. Fourier-transform infrared spectroscopy (FTIR) analysis confirmed that the carbonate rock materials collected from Kunduchi were calcite containing a small amount of silica/quartz. It was also found that the rock materials sourced from Kwamsisi (in Tanga) were dolostone containing near-stoichiometric dolomite as the primary mineral. On the other hand, the materials obtained from Merelani (Manyara) were found to be dolostone containing non-stoichiometric dolomite; magnesium deficient dolomite. Atomic pair distribution function (PDF) fitting confirmed that the rock materials collected from Merelani contain dolomite and a small amount of calcite mineral.

The as-mined Pugu clay was found to contain kaolinite mineral as confirmed by the presence of the minerals' diagnostic peaks on the FTIR spectrum. This is consistent with the findings of Sempeho *et al.* (2015), where beneficiated Pugu clay was found to contain kaolinite as the main aluminum phyllosilicate mineral. Also, it is evident that the clay material used in this study is indeed Kaolin containing significant amount silica, iron and magnesium compounds (as shown by XRF elemental analysis).

### 4.2 Characterization of the Synthesized Material

#### 4.2.1 Fourier-Transform Infrared Spectroscopy

The FTIR spectra of the synthesized material powders, sintered at the annotated temperatures, are shown in Fig. 11. Table 7 presents the selected FTIR band/peaks extracted from the spectra. Due to overlapping with clay peaks, the majority of the peaks assignable to phosphate groups in the K:R = 75:25 did not feature distinctly (FTIR data for sintered K:R = 75:25 are not presented). The band ascribable to $CO_3^{2-}$, however, could still be identified despite the overlapping (Fig. 12). The main bands at 1000 – 1150 $cm^{-1}$ correspond to the asymmetric stretching mode of $PO_4^{3-}$ groups ($\nu_3$ $PO_4$). The shoulder 963.5 ± 0.5 $cm^{-1}$ is ascribed to the symmetric stretching ($\nu_1$ $PO_4$) The shoulder at 963.5 ± 0.5 $cm^{-1}$ is ascribed to the symmetric stretching ($\nu_1$ $PO_4$) while the less intense bands at 603 - 582 $cm^{-1}$ and 560 – 550 $cm^{-1}$ (variations due to temperature change) are due to the bending mode of $PO_4^{3-}$ groups ($\nu_4$ $PO_4$) (Kabir, Ahmed, Mustafa, Ahsan & Islam, 2012) (Table 9). The weak but broad band between 3442

$cm^{-1}$ and 1644 $cm^{-1}$ corresponds to O–H stretching from adsorbed water. The material exhibits a band at 963 $cm^{-1}$ (Berzina-Cimdina & Borodajenko, 2012).

According to Drouet (2013) a band at 962 ± 2 $cm^{-1}$ assignable to $\nu_1$ ($PO_4$) is observed in apatite phases or OCP but not in ACP, monetite and brushite (Drouet, 2013) (K: R=0: 100). In this work, the band was observed at 963.5 ± 0.5 $cm^{-1}$ band. Since the band was not accompanied by other OCP characteristic bands (1195 $cm^{-1}$ and 916 $cm^{-1}$) it is logical to assume that the band is largely due to the apatite phase. The band (963.5 ± 0.5 $cm^{-1}$) diminished with an increase in temperature, disappearing at 700 $^{o}$C. It was replaced by new peaks at 987 $cm^{-1}$ (600 °C), 985 $cm^{-1}$ (800 °C), 990 $cm^{-1}$ (800 °C) and 947 $cm^{-1}$ (900 °C) (Table 9) which are assignable to β-TCP. The bands for β-TCP have been reported to be located at 946 – 943 $cm^{-1}$ 975 – 970 $cm^{-1}$ and 984 $cm^{-1}$.

There was no clear detection of apatitic $OH^-$ bands at around 3570 $cm^{-1}$ and 630 $cm^{-1}$ to signify the presence of hydroxylapatite. This, however, does not confirm the absence of hydroxylapatite, though it may indicate low levels of structural $OH^-$. Literature shows that nonstoichiometry and ionic substitution disfavor the presence of $OH^-$ ions in apatite channels leading to vacant sites (Antonakos, Liarokapis & Leventouri, 2007; Drouet, 2013; Prekajski *et al.*, 2016). Fleet and Liu (2007) observed that increasing carbonate content resulted in a progressive reduction in intensity, and eventually total disappearance, of the $OH^-$ stretch and vibration bands at 3570 $cm^{-1}$ and $OH^-$ bands at 631 $cm^{-1}$ respectively. Yakub and Soboyejo (2013).

The bands between 1380-1545 $cm^{-1}$, with poorly resolved peaks at 1434 $cm^{-1}$ (unsintered), 1450 $cm^{-1}$ (at 500 °C and 600 °C), and 1460 $cm^{-1}$ (700 °C) indicate the presence of carbonate ($CO_3^{2-}$). The bulging band at around ~880 $cm^{-1}$ ($\nu_2$ $CO_3^{2-}$) further attests to the presence of $CO_3^{2-}$. Ren and Leng (2012) asserts that the bands at ~880 $cm^{-1}$, ~1420 $cm^{-1}$, and~1450 $cm^{-1}$ should not be used to identify carbonated apatite as they may result from carbonate adsorbed on surfaces of apatite crystals or separate carbonate phase present with apatite crystals. It was suggested that IR characteristic bands of carbonate substitution in apatites should be: $\nu_3$ band at ~1546 $cm^{-1}$ for type-A and $\nu_3$ band at ~1465 $cm^{-1}$ for type-B. Although the apatitic carbonate peak was not distinct (in both K:R = 0:100 and K:R = 75:25), possibly due to overlapping in a wide bands between 1375 $cm^{-1}$ and 1550 $cm^{-1}$, the absence (or low level) of $OH^-$ when apatite is present (963.5 ± 0.5 $cm^{-1}$) suggests type-A carbonate substitution.

The broad band at 750 $cm^{-1}$ was assigned to pyrophosphate group ($P_2O_7^{4-}$). In other studies the band has been observed at 715 $cm^{-1}$ (Toibah, Sopyan, Yuhazri, Jeefferie & Nooririnah, 2012), 725 $cm^{-1}$ (Berzina-Cimdina and Borodajenko, 2012) and 740 - 720 $cm^{-1}$ (Gozalian, Behnamghader, Daliri & Moshkforoush, 2011). Gozalian *et al.* (2011) observed that the pyrophosphate band disappeared from the spectrum of the materials sintered 800 ℃. In this study, the band progressively diminished in intensity with an increase in temperature and disappeared at 800 ℃. This suggests that $P_2O_7^{4-}$ (possibly magnesium substituted, $MgCaP_2O_7$, MgCPP) decomposes at temperatures between 500 ℃ and 700 ℃. Also, another peak at 963.5 ± 0.5 $cm^{-1}$, assignable to the apatite phase, diminished with an increase in temperature and disappeared at 700 ℃. The concurrent decrease in intensity of the band at 750 $cm^{-1}$ and that at 963.5 ± 0.5 $cm^{-1}$ suggests a reaction between the apatite phase and the pyrophosphate phase to yield β-TCP (Shiryaev *et al.*, 2010).

Figure 12 presents FTIR spectra of K:R = 0:100 (Ca/Mg phosphate), K:R = 75:25 (Clay-Mg/Ca phosphate composite) and K:R = 100:0. Some major peaks in the spectra of K:R = 0:100 and K:R = 100:0 are observed in K:R = 75:25 (Clay). This shows successiful in-situ formation of calcium phosphate system in the clay matrix.

**Table 7: Observed FTIR bands/Peaks (in $cm^{-1}$) of K:R = 0:100 sintered at the specified temperatures**

| Un-sintered | 500 ℃ | 600 ℃ | 700 ℃ | 800 ℃ | 900 ℃ | Assignments |
|---|---|---|---|---|---|---|
| 483 | 483 | 483 | 485 | 484 | 485 | $PO_4^{3-}$ bending ($\nu_2$) |
| 562 | 560 | 560 | 554 | 554 | 561 | $PO_4^{3-}$ bending ($\nu_4$) |
| 601 | 602 | 603 | 599 | 596 | 582 | $PO_4^{3-}$ bending ($\nu_4$) |
| 750 | 750 | 750 | 751 | - | - | $P_2O_7^{4-}$ |
| 880 | 889 | 879 | - | - | - | $CO_3^{2-}$ group/$HPO_4^{2-}$ |
| ~965 | 965 | 963 | - | - | - | $PO_4^{3-}$ stretching ($\nu_1$) |
| - | - | ~987 | 987 | 987 | 990 | β-TCP, $PO_4^{3-}$ bending ($\nu_3$) |
| - | - | - | - | ~949 | 945 | β-TCP, $PO_4^{3-}$ bending ($\nu_3$) |
| 1019 | 1020 | 1020 | 1021 | 1023 | 1023 | $PO_4^{3-}$ bending ($\nu_3$) |
| ~1056 | ~1053 | ~1053 | ~1053 | ~1053 | ~1053 | $PO_4^{3-}$ bending ($\nu_3$) |
| ~1114 | 1116 | 1116 | 1116 | 1116 | ~1116 | $PO_4^{3-}$ bending ($\nu_3$) |
| 1422 | 1438 | 1432 | 1425 | 1423 | - | $CO_3^{2-}$ group |
| 1450 | 1450 | 1450 | - | - | - | $CO_3^{2-}$ group |
| 1623 | 1623 | - | - | - | - | water absorbed ($\nu_2$) |

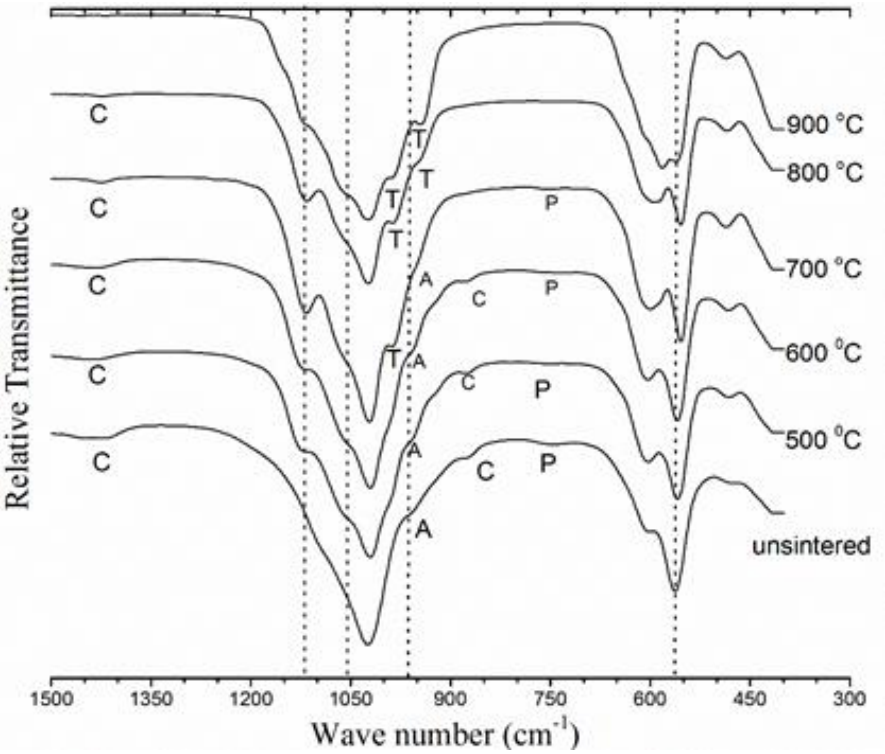


**Figure 11: FTIR spectrum of K:R = 0:100 sintered at the annotated temperature; A stands for apatite phase, C is carbonate group, P is pyrophosphate and T is β-tricalcium phosphate**

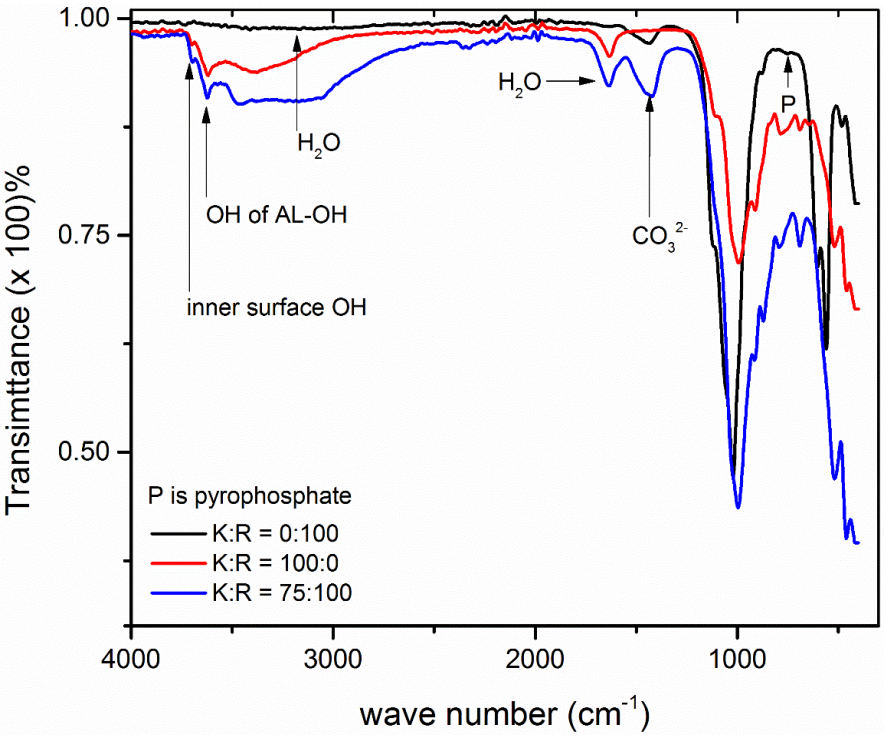


**Figure 12: FTIR spectra of K:R = 0:100, K:R = 75:25 and K:R = 85:15**

### 4.2.2 Fourier-Transform Infrared Spectroscopy Analysis

Figure 13 (a) and (b) shows diffractograms of K:R = 0:100 and K:R = 75:25 respectively, sintered at the annotated temperatures. The PDF modeling indicated the presence of brushite ($CaHP_2O_4.2H_2O$), apatite (possibly magnesium-substituted carbonate apatite, MgCAp), octacalcium phosphate (OCP) (also possibly cationic substituted) and monetite. Table 8 summarizes lattice parameters and other structural information of the unsintered and sintered K:R = 0:100, that point to these phases. In the table "D" stands for the diameter in the spherical characteristic function, "scale" is the scale factor of the PDF of each phase, "$\delta_2$" is the quadratic correction for correlation motion of atoms, the "a", "b" and "c" are the lattice constants and is "$U_{iso}$" is the isotropic displacement parameter. The presence of ACP, is shown by the hump on the diffractogram. Other phases which could be present include newberyite ($MgHPO_4.3H_2O$) and whitlockite ($Ca_9(MgFe)(PO_4)_6PO_3OH$).

The sintering temperature does affect the phases inside the product. This is clearer in Fig. 13, which shows changes in the PDFs as sintering temperatures increases, with the 500 ℃ sintering already producing significant modifications compared to the unsintered samples. Crystallite size as a function of sintering temperature can be assessed by directly looking at the PDF when it is plotted over a wide range of r (Fig. 14). The more crystalline samples, with the same structure, show slower damping of their PDFs with increasing r and higher amplitude oscillations (signal) in the high-r region. Careful inspection of Fig. 14(a) and (b) reveal that crystallinity is slightly reduced on sintering at 500 ℃ compared to the unsintered sample. However, higher sintering temperatures resulted in the growth of crystallite size. The crystallite growth effect is not as evident in the clay containing material (K:R = 75:25), Fig. 14 (b). In both cases, (K:R = 0:100 and K:R = 75:25) distinct increase in crystallinity occurs at 700 ℃ (Fig. 13 and Fig. 14).

The diffractograms in Fig. 13 show the disappearance of some peaks at 500 ℃. These peaks are due to brushite, OCP and, possibly, newberyite peaks. This is expected as according to literature, the phases condensed to pyrophosphates (Dosen & Giese, 2011; Karampas & Kontoyannis, 2013).

Literature shows that at elevated temperature hydroxylapatite (Hap) reacts with pyrophosphates to form β-TCP (Shiryaev *et al.*, 2010). Also, previous studies have shown that, at elevated temperature ( 600–720 ℃), ACP transforms into metastable crystalline phases such

as $Ca_3(PO_4)_2$ (TCP) and $Ca_2P_2O_7$ (CPP) which at around 800 °C transform into their more stable forms, β-CPP and β-TCP (Maciejewski, Brunner, Loher, Stark & Baiker, 2008; Minh, Martinez, Nzihou & Sharrock, 2013; Somrani, Rey & Jemal, 2003; Vecstaudza, Gasik & Locs, 2019; Zyman *et al.*, 2017). In this study, PDF analysis indicates the presence of β-CPP and β-TCP beginning as early as 600 °C (Table 10). The formation of the β-TCP phases at a lower temperature than expected may be attributed to the destabilization of the precursor phases (ACP, CPP and apatite) caused by $Mg^{2+}$ substitutions and other cations. The presence of β-TCP is also evidenced by FTIR results (Table 7). The shoulder at 987 ± 2 $cm^{-1}$ (at 500 - 900 °C), which is more distinct for the materials sintered at 700 °C, but begins to appear as a perceptible shoulder at 500 °C, supports the presence of β-TCP in the materials. On the other hand, material K:R = 75:25 increase in disorder seems to be the dominant change as sintering temperature elevates. The increase in the disorder could be due to the collapse of the clay mineral structure (aluminum phyllosilicate structure).

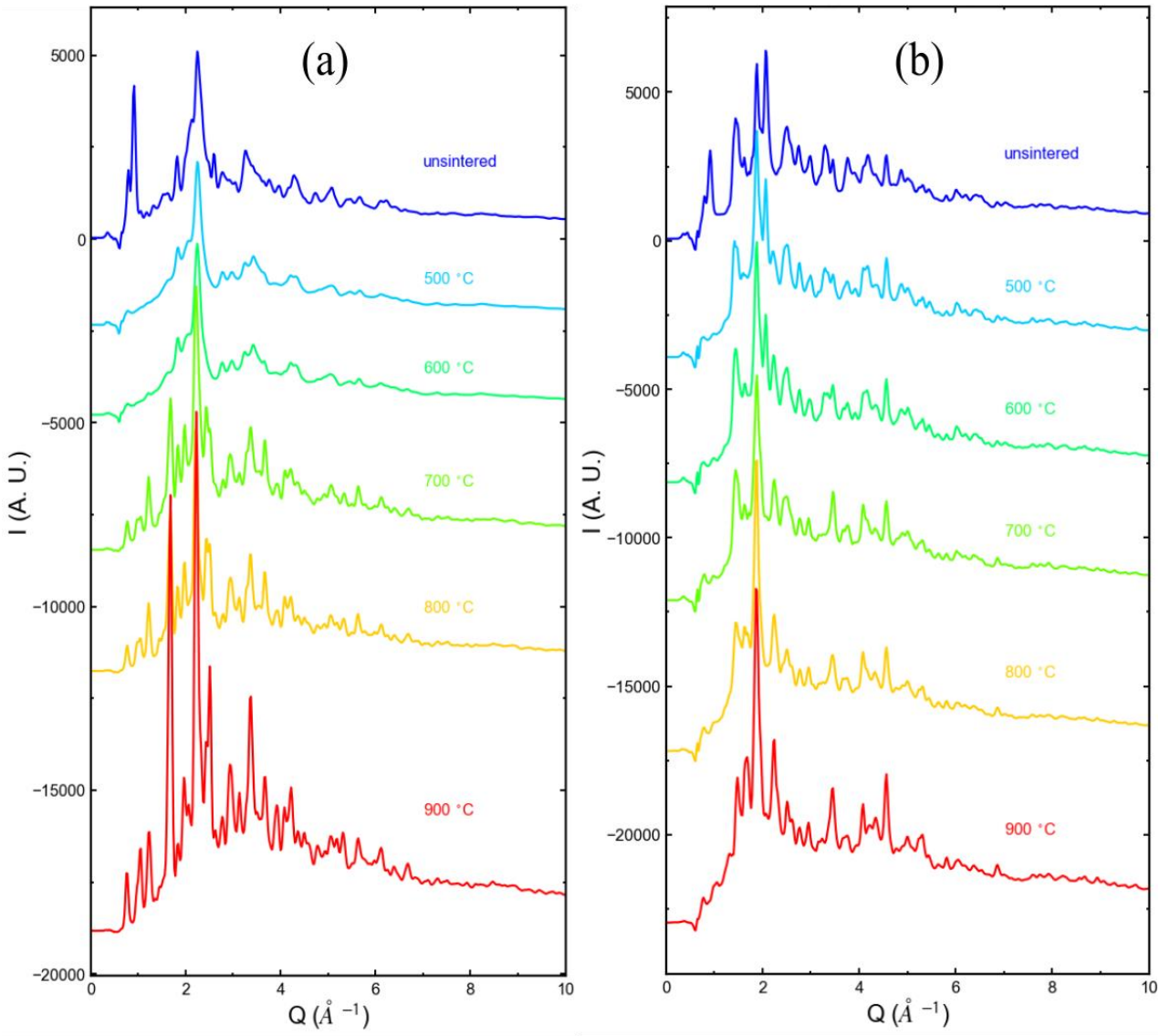


**Figure 13: Diffractograms of K:R= 0:100 (a) and K:R = 75:25 (b) sintered at various temperatures**

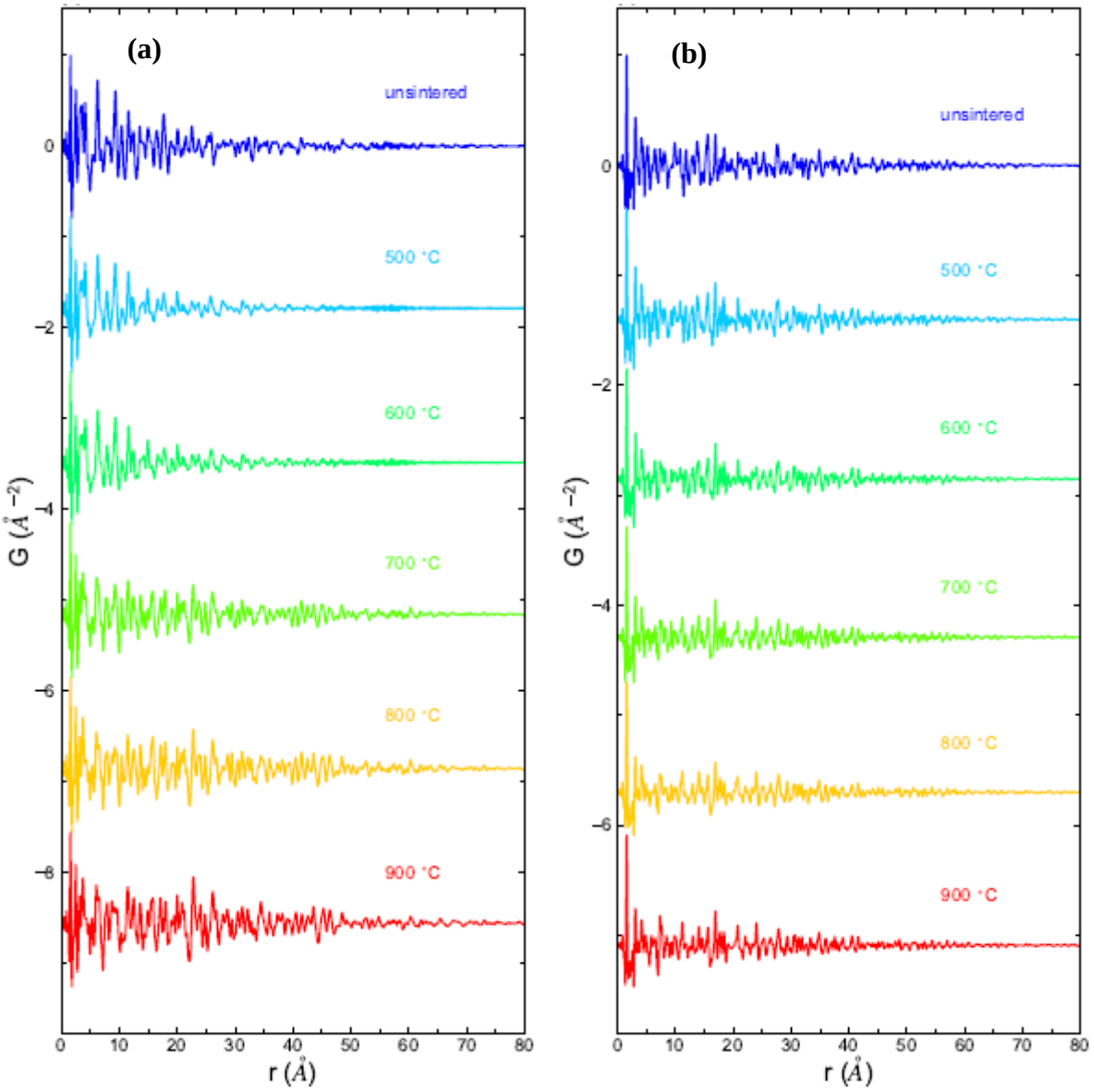


**Figure 14: The measured PDFs of samples produced in K:R = 0:100 (a) and K:R = 75:25 (b). The range is from 0 Å to 80 Å. The sintering temperature of each sample is annotated on the upper right side of each curve**

**Table 8: The atomic pair distribution function (PDF) fitting results of the K:R = 0:100**

| | Un-sintered | 500 ºC | 600 ºC | 700 ºC | 800 ºC | 900 ºC |
|---|---|---|---|---|---|---|
| Beta tricalcium phosphate | | | | | | |
| D (Å) | N/A | N/A | 14.972 | 85.912 | 85.912 | 85.912 |
| Scale | N/A | N/A | 0.005 | 0.046 | 0.056 | 0.025 |
| $\delta_2$ (Å$^2$) | N/A | N/A | 2.364 | 2.295 | 3.296 | 3.297 |
| a | N/A | N/A | 10.455 | 10.301 | 10.321 | 10.339 |
| c | N/A | N/A | 37.702 | 37.075 | 37.075 | 37.035 |
| $U_{iso}$(Ca)(Å$^2$) | N/A | N/A | 0.006 | 0.004 | 0.002 | 0.001 |
| $U_{iso}$(O)(Å$^2$) | N/A | N/A | 0.003 | 0.003 | 0.002 | 0.002 |
| $U_{iso}$(P)(Å$^2$) | N/A | N/A | 0.004 | 0.004 | 0.004 | 0.003 |
| Beta tricalcium pyrophosphate | | | | | | |
| D (Å) | N/A | 44.321 | 40.769 | 53.975 | 53.976 | 53.976 |
| Scale | N/A | 0.077 | 0.049 | 0.049 | 0.072 | 0.064 |
| $\delta_2$ (Å$^2$) | N/A | 2.054 | 2.238 | 2.164 | 2.246 | 2.237 |
| a | N/A | 12.362 | 12.316 | 12.214 | 12.254 | 12.251 |
| b | N/A | 9.285 | 9.285 | 9.404 | 9.458 | 9.492 |
| c | N/A | 6.767 | 6.714 | 6.536 | 6.465 | 6.425 |
| β(deg) | N/A | 107.003 | 106.705 | 104.709 | 104.789 | 104.828 |
| $U_{iso}$(Ca)(Å$^2$) | N/A | 0.017 | 0.013 | 0.019 | 0.019 | 0.019 |
| $U_{iso}$(O)(Å$^2$) | N/A | 0.017 | 0.013 | 0.005 | 0.004 | 0.005 |
| $U_{iso}$(P)(Å$^2$) | N/A | 0.005 | 0.004 | 0.02 | 0.02 | 0.019 |
| Hydroxylapatite | | | | | | |
| D (Å) | 355.775 | 318.937 | 300.401 | 235.364 | N/A | N/A |
| Scale | 0.37 | 0.052 | 0.052 | 0.004 | N/A | N/A |
| $\delta_2$ (Å$^2$) | 1.131 | 2.045 | 2.03 | 2.093 | N/A | N/A |
| a | 9.437 | 9.407 | 9.441 | 9.441 | N/A | N/A |
| c | 6.848 | 6.929 | 6.946 | 6.962 | N/A | N/A |
| $U_{iso}$(Ca)(Å$^2$) | 0.01 | 0.01 | 0.009 | 0.015 | N/A | N/A |
| $U_{iso}$(O)(Å$^2$) | 0.009 | 0.013 | 0.011 | 0.06 | N/A | N/A |
| $U_{iso}$(P)(Å$^2$) | 0.008 | 0.02 | 0.02 | 0.04 | N/A | N/A |
| Brushite | | | | | | |
| D (Å) | 51.937 | N/A | N/A | N/A | N/A | N/A |
| Scale | 0.024 | N/A | N/A | N/A | N/A | N/A |
| $\delta_2$ (Å$^2$) | 2.655 | N/A | N/A | N/A | N/A | N/A |
| a | 5.854 | N/A | N/A | N/A | N/A | N/A |
| b | 15.322 | N/A | N/A | N/A | N/A | N/A |
| c | 6.362 | N/A | N/A | N/A | N/A | N/A |
| β(deg) | 116.332 | N/A | N/A | N/A | N/A | N/A |
| $U_{iso}$(Ca)(Å$^2$) | 0.007 | N/A | N/A | N/A | N/A | N/A |

| | Un-sintered | 500 ºC | 600 ºC | 700 ºC | 800 ºC | 900 ºC |
|---|---|---|---|---|---|---|
| $U_{iso}$(O)(Å$^2$) | 0.04 | N/A | N/A | N/A | N/A | N/A |
| $U_{iso}$(P)(Å$^2$) | 0.05 | N/A | N/A | N/A | N/A | N/A |
| Octacalcium phosphate (OCP) | | | | | | |
| D (Å) | 98.378 | N/A | N/A | N/A | N/A | N/A |
| Scale | 0.098 | N/A | N/A | N/A | N/A | N/A |
| $\delta_2$ (Å$^2$) | 2.132 | N/A | N/A | N/A | N/A | N/A |
| a | 19.334 | N/A | N/A | N/A | N/A | N/A |
| b | 9.516 | N/A | N/A | N/A | N/A | N/A |
| c | 6.776 | N/A | N/A | N/A | N/A | N/A |
| α(deg) | 88.932 | N/A | N/A | N/A | N/A | N/A |
| β(deg) | 92.828 | N/A | N/A | N/A | N/A | N/A |
| $U_{iso}$(Ca)(Å$^2$) | 105.729 | N/A | N/A | N/A | N/A | N/A |
| $U_{iso}$(O)(Å$^2$) | 0.004 | N/A | N/A | N/A | N/A | N/A |
| $U_{iso}$(P)(Å$^2$) | 0.05 | N/A | N/A | N/A | N/A | N/A |

### 4.2.3 Thermogravimetric Analysis

Figure 15 shows the TG curves of the material K:R = 0:100 and K:R = 75:25, on heating process at a rate of 10C/min, from room temperature to 900 ℃. The curves show a continuous loss of weight with three distinct weight drops, K:R = 0:100 (region A', B' and C') and K:R = 75:25 (region A, B and C). The continuous loss could be due to escaping surface water and, at high temperature, carbon dioxide. The first two weight drop steps are characteristic of brushite ($CaHPO_4$. $2H_2O$) and newberyite ($MgHPO_4$. $3H_2O$).

Literature shows that, when heated, brushite ($CaHPO_4$. $2H_2O$) and newberyite ($MgHPO_4$. $3H_2O$) lose structural water in two steps to yield pyrophosphates. The first step, which is reported to occur at 120 - 220 ℃, leads the formation of anhydrous monetite (dicalcium phosphate anhydrous DCPA, $CaHPO_4$) and MgHPO4 (dehydrated newberyite) (Anastasiou *et al.*, 2016; Dosen and Giese, 2011). The second step, which occurs at 350 - 500 ℃, involves the removal of a proton from the monetite and $MgHPO_4$ (metaphases) to form calcium pyrophosphate (Anastasiou *et al.*, 2016; Dosen and Giese, 2011).

In this work, the distinct weight loss at A and A' (at ~130 - 175 ℃, region A for K:R = 75:25 and at ~125 - 170 ℃ , region A' for K:R = 0:100 ) corresponds to the first dehydration step while the loss at B and B'(at 365-400 ℃) for K:R = 0:100 and around 334 ℃ for K:R = 75:25)

matches the second step of the dehydration process. The second step may have lead to formation of magnesium-substituted calcium pyrophosphate (γ-$CaMgP_2O_7$). Also, octacalcium phosphate (OCP, $Ca_8H_2(PO_4)_6$. $5H_2O$) is known to lose water in the temperature range between 75 ℃ and 150 ℃ depending on structural inclusions present (Sugiura and Makita, 2018). Another possible phase that can undergo dehydration in this range of temperature is hydrated magnesium-substituted calcium pyrophosphates ($MgCaP_2O_7$. $xH_2O$, MgCPP), where x stands for the number of water molecules. These dehydration reactions evidence the presence of one or more of these phases (brushite, newberyite and OCP), in addition to ACP (as evidenced by PDF analysis).

The other distinct mass drop more pronounced in K:R = 75:25, at a temperature between ~620 ℃ and ~660 ℃ (region C and C' in Fig. 15) could be due to dehydroxylation of the apatite phase. The higher pronouncement of region C in K:R = 75:25 suggests higher apatite content than in K:R = 0:100 The TGA results, therefore, suggest the presence of brushite and/or newberyite, and apatite phase in the un-sintered material, complementing FTIR and PDF analysis results.

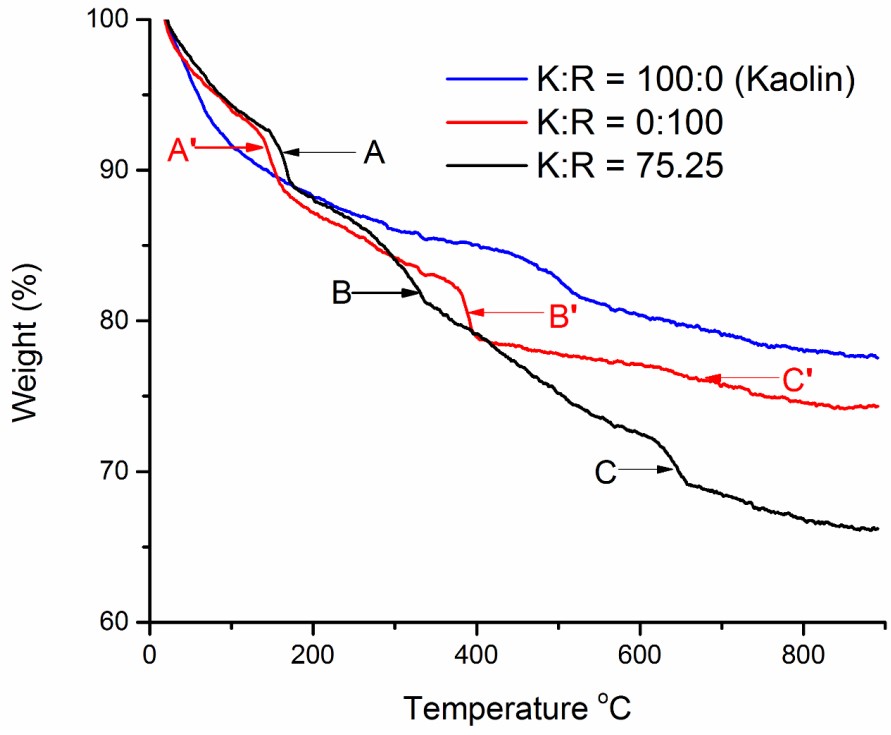


**Figure 15: TGA analysis of K:R = 0:100, K:R = 75:25 and K:R = 100:0**

## 4.3 Summary of the Characterization of the Synthesized Materials

The synthesized materials were characterized by FTIR, TGA and XRD. Fourier-transform infrared spectroscopy (FTIR) results suggested the presence of highly substituted hydroxylapatite as one of the components of the material, though may not be the dominant phase. The peak at 963.5 ± 0.5 $cm^{-1}$ was used as evidence of the presence of the apatite phase. Although the apatite $CO_3^{2-}$ peak was not distinct due overlapping in a wide band (1375 - 1550 $cm^{-1}$), the absence of $OH^-$ when the apatite phase is present suggests type A carbonate substitution. It can also be seen on the FTIR spectra (Fig. 11) that carbonate content decreased with increase in temperature. As sintering temperature increased, some peaks/bands were replaced by new ones (Fig. 11 and Table 7) indicating phase transformation, with the effect being more pronounced at 700 ℃. The concurrent decrease in intensity, and eventually the disappearance, of the band for the apatite phase at 963.5 ± 0.5 $cm^{-1}$ and that of pyrophosphates at 750 $cm^{-1}$ at 700 ℃ suggest a reaction between the phases yielding β-TCP (magnesium-substituted β-TCP). Thermogravimetric analysis (TGA) indicated the presence of phases that lose water in two stages at relatively low temperatures. This is strong evidence that the synthesized material contains one or more of the following phases; brushite, monetite, newberyite and octacalcium phosphate. The atomic pair distribution function (PDF) analysis confirmed the presence apatite, brushite and amorphous phase in the unsintered K:R = 75:25 and K:R = 0:100. For the sintered materials, PDF analysis confirmed the presence of β-TCP, pyrophosphate and residual dolomite.

## 4.4 De-fluoridation Activity Testing of the Synthesized Ca/Mg Phosphate Systems

### 4.4.1 Fluoride Adsorption by Pellets

Table 9 presents fluoride adsorption results of porous clay ceramic pellets containing *in-situ* generated Ca/Mg phosphate system sintered at 600 ℃. The adsorption experiments were carried out using 50 mL of 10 mg/L simulated fluoride-water. It can be seen that the three composite ceramic materials show promising de-fluoridation results. The results show that heat pre-treated carbonate rock materials can be used as a source of Ca/Mg in the synthesis of porous clay ceramics containing *in-situ* generated Ca/Mg phosphate system (clay-Ca/Mg phosphate composite ceramic). The differences in de-fluoridation performance of the synthesized material may be attributed to the variations in Ca/Mg content and the fluoride adsorption properties of impurities. The adsorbent synthesized using dolostone collected from Tanga (near-

stoichiometric dolomite) exhibited lower de-fluoridation performance than one prepared using the Merelani dolostone (non-stoichiometric Mg deficient dolomite), possibly due to higher quartz/silica (see XRF and FTIR results) and Magnesium content (FTIR results) in the later. The magnesium and other impurities could be interfering with the formation of phosphate system, leading to a product with relatively inferior fluoride adsorption properties. Also, the higher silicon content in the Kunduchi limestone could account for the lower de-fluoridation activity of the resultant adsorbent compared to the Merelani dolostone. It was interesting to learn that, even with higher silica/quartz content, adsorbent synthesized using Kunduchi limestone ($CaCO_3$) still had higher de-fluoridation performance than the one synthesized using Tanga dolostone; containing largely near-stoichiometric dolomite (FTIR and XRD results), collected from Merelani. This suggests that high magnesium content affects the nature of the resultant adsorbent such that its de-fluoridation activity is low. Based on the de-fluoridation performance results in Table 9, the Merelani dolostone (containing mainly magnesium-deficient dolomite) was used in the subsequent studies.

**Table 9: De-fluoridation efficiency obtained using 2 g of the adsorbent pellets per 50 mL of 10 mg/g $F^-$, synthesized using the specified Ca/Mg sources**

| Precursor rock material (major mineral) | Initial pH | Final pH | De-fluoridation efficiency % |
|---|---|---|---|
| Tanga dolostone (Near-stoichiometric dolomite) | 7.4 | 10.2 ± 3 | 91.7 ± 4 |
| Merelani dolostone (Magnesium deficient dolomite) | 7.4 | 10.4 ± 2 | 97.8 ± 2 |
| Kunduchi (Limestone) | 7.4 | 9.9 ± 2 | 95.2 ± 3 |

### 4.4.2 Adsorption Isotherms; Comparison Between Freundlich and Langmuir Model, and the Determination of De-fluoridation Capacity

Experimental data show that increasing adsorbent material (material dose) while keeping fluoride concentration constant leads to increased de-fluoridation efficiency and reduced de-fluoridation amount. The amount of fluoride adsorbed at equilibrium per mass of material used ($q_e$, in mg/g), and the fluoride concentration at equilibrium ($C_e$, mg/L) for a weight range of adsorbent materials was obtained. Langmuir and Freundlich isotherm models (Equation 9 and 11) were used to study the material. Freundlich constants were obtained from plots of $\ln q_e$ versus $\ln C_e$. Freundlich de-fluoridation capacity ($Q_m$) was determined using equation 12 which is derived from equation 10.

$$Q_{max} = K_f C_o^{1/n} \quad (12)$$

Where $K_f$ and 1/n are obtained from the intercept and slope of the graph of $\ln q_e$ versus $\ln C_e$ (Equation 11). $C_o$ is the initial fluoride concentration in mg/L. Maximum de-fluoridation capacity ($Q_m$) for the Langmuir model was calculated as the inverse of the slope of the plot $C_e/q_e$ versus $C_e$

Figure 16 presents Freundlich and Langmuir isothermal plots of K:R = 75:25 and K:R = 85:15 sintered at 700 ℃, to illustrate the fitting of the adsorption data. Also, Table 10 presents some of the parameters extracted from Freundlich and Langmuir model plots of K:R = 75:25, K:R = 85:15 and K:R = 90:10. It was found that, despite giving high $R^2$, Langmuir model could not describe the data. For instance, while Freundlich model predicted $Q_m$ of 3.2 mg/g for the adsorbent K:R = 75:25, which is slightly higher than the experimental $q_e$ value (2.8 mg/g) afforded by the smallest dose used in the adsorption tests, Langmuir returned an unrealistic value of 0.25 mg/g for the same data (Table 10). It is therefore evident, from the comparison between the parameters extracted from Freundlich and Langmuir plots (Table 10), that the data is described by Freundlich model. Langmuir model also returned unrealistic $Q_m$ values for the rest of the adsorbent materials ( K:R = 85:25, 75:15 and 85:10 sintered at 700 ℃ ) Table 12 shows that the model does not describe the data.

| Freundlich isotherm plot | Langmuir isotherm plot |
| --- | --- |
| 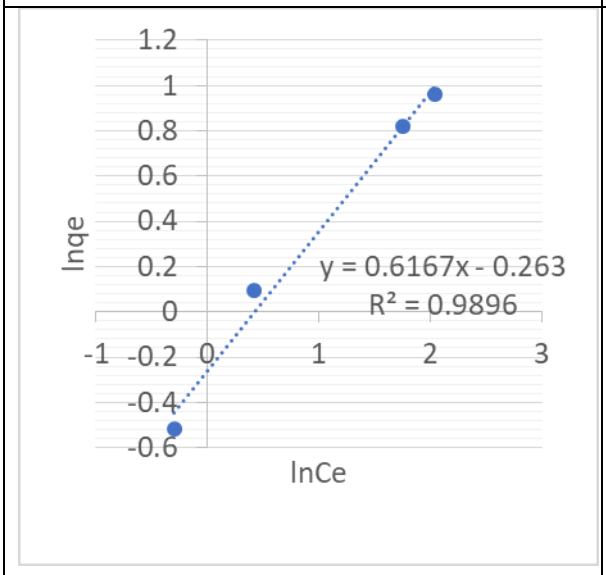 | 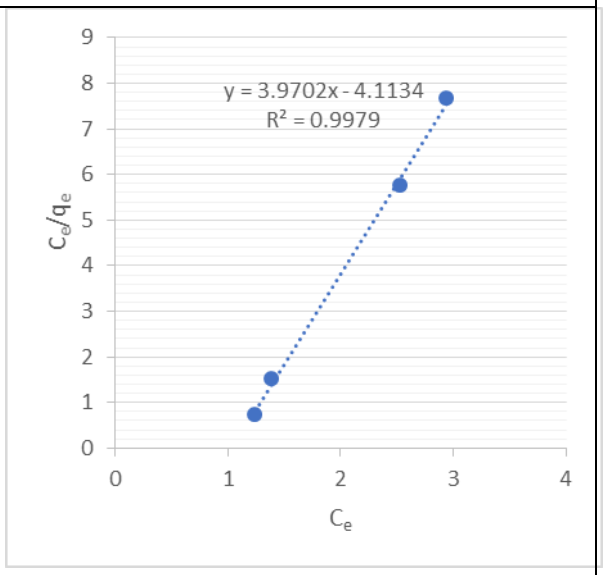 |
| 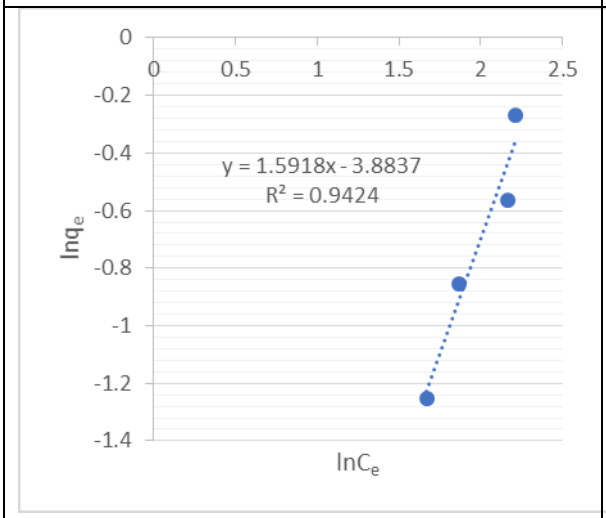 | 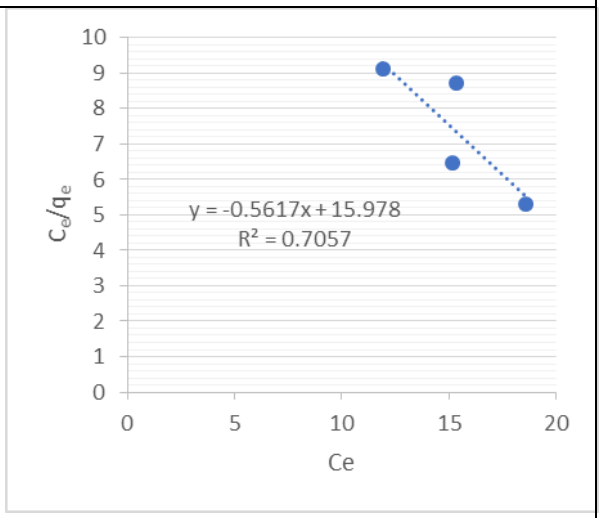 |

**Figure 16: Freundlich and Langmuir plots of K:R = 75:25, K:R = 85:15 and K:R = 90:10, sintered at 700 ℃ to demonstrate**

**Table 10: Selected Freundlich and Langmuir isothermal parameters of K:R = 75:25, K:R = 85:15 and K:R = 90:10, sintered at 700 ℃. Langmuir model returns unrealistic Qm values**

| K:R = 75:25 | **Symbol** | **Freundlich** | **Langmuir** |
|---|---|---|---|
| | $R^2$ | 0.98 | 0.99 |
| | $Q_m$ | 3.24 | 0.25 |
| | $K_f$ | 0.712 | |
| | 1/n | 0.621 | |
| | $K_L$ | | -0.07 |
| K:R = 85:15 | | | |
| | $R^2$ | 0.94 | 0.71 |
| | $Q_m$ | 0.79 | 1.78 |
| | $K_f$ | 0.021 | |
| | 1/n | 1.59 | |
| | $K_L$ | | 0.035 |
| K:R = 90:10 | | | |
| | $R^2$ | 0.75 | 0.57 |
| | $Q_m$ | 0.29 | 26.32 |
| | $K_f$ | 0.01 | |
| | 1/n | 2.688 | |
| | $K_L$ | | 0.0008 |

Since the Langmuir model failed to describe the data, the Freundlich isotherm model was used to study all the materials synthesized in this work. Table 11 presents Freundlich isotherm parameters, adsorption capacity and free energy of all adsorbents except K:R = 95:5 which did not also obey the Freundlich model. Table 10 and Table 11, show that $Q_m$ decreases as dolostone fraction is reduced leading to decrease in de-fluoridation activity. The correlation coefficient obtained from the Freundlich fits of materials K:R=0:100, K:R = 75:100 and K:R = 0:100 were approximately 0.71 – 0.99. An adsorption system described by the Freundlich model is known to have an adsorbent with heterogeneous adsorption sites onto which multi-layer adsorption may also occur. The synthesized material in this study is, therefore, heterogeneous capable of allowing multilayer adsorption. This violates the fundamental assumption of the Langmuir isotherm in that all of the adsorption sites have equal affinities for adsorbate molecules.

**Table 11: Freundlich isotherm parameters and Gibbs free energy**

| Adsorbent | Sintering Temperature | Freundlich Isotherm Parameters | | | | Change in Free Energy |
|---|---|---|---|---|---|---|
| | T (℃) | $K_f$ (mg/g·min$^{1/2}$) | 1/n | $R^2$ | $Q_m$ (mg/g) | ΔG (kJ/mol) |
| K:R = 0:100 | | | | | | |
| | 500 | 0.009 | 2.52 | 9.68 | 2.26 | 6.86 |
| | 600 | 0.081 | 1.44 | 0.94 | 2.28 | 6.70 |
| | 700 | 0.069 | 1.58 | 0.93 | 2.60 | 4.94 |
| | 800 | 0.039 | 0.49 | 0.92 | 1.20 | 2.37 |
| | 900 | 0.120 | 2.38 | 0.85 | 2.89 | 2.38 |
| K:R = 75:25 | | | | | | |
| | 500 | 0.7287 | 0.416 | 0.98 | 2.82 | 0.35 |
| | 600 | 0.7687 | 0.616 | 0.98 | 3.2 | 0.35 |
| | 700 | 0.7124 | 0.621 | 0.98 | 3.24 | 0.39 |
| | 800 | 0.1251 | 1.138 | 0.99 | 1.64 | 4.97 |
| | 900 | 0.5503 | 1.18 | 0.91 | 1.7 | 1.29 |
| K:R = 85:15 | | | | | | |
| | 500 | 0.182 | 1.65 | 0.89 | 2.82 | 3.98 |
| | 600 | 0.1302 | 1.85 | 0.89 | 1.54 | 4.6 |
| | 700 | 0.0206 | 1.59 | 0.94 | 0.79 | 8.24 |
| | 800 | 0.0011 | 1.35 | 0.93 | 0.38 | 9.8 |
| | 900 | 0.02 | 1.51 | 0.85 | 0.63 | 8.6 |
| K:R = 90:10 | | | | | | |
| | 500 | 0.018 | 3.122 | 0.88 | 0.17 | 11.33 |
| | 600 | 0.008 | 0.232 | 0.84 | 0.32 | 6.544 |
| | 700 | 0.001 | 2.688 | 0.75 | 0.29 | 0.618 |
| | 800 | 1.35E-10 | 9.533 | 0.85 | 0.21 | 30.99 |
| | 900 | 6.04E-11 | 9.389 | 0.76 | 0.13 | 32.67 |

### 4.4.3 Change in Free Energy

Change in free energy of the adsorbent - fluoride system was determined from the following expression (Equation 13):

$$\Delta G = -RT \ln K_o \qquad (13)$$

where ΔG (kJ/mol) is the change in free energy; R (8.314 $Jmol^{-1}K^{-1}$) is the universal gas constant; T (Kelvin) is absolute temperature; and $K_o$ is the thermodynamic distribution coefficient for the adsorption process. The writers determined $K_o$ from the intercept of the plot of $\ln(q_e/C_e)$ against $C_e$. The positive values for free energy indicate that the adsorption process is endothermic; non-spontaneous. It is, therefore, logical to conclude that the process obtained its energy requirements from the environment. However, there was no clear trend in the dependence of free energy on sintering temperature for all other adsorbent types.

### 4.4.4 Effect of Sintering Temperature on Fluoride Adsorption

Figure 17 and 18 present graphs depicting how de-fluoridation performance of K:R = 0:100 and K:R = 75:25, vary with sintering temperature. The graphs also serve to show that fluoride removed at equilibrium (de-fluoridation amount) decreases with increase in adsorbent dose. Similar trends were observed for the other adsorbents that were treated in the same $F^-$ concentration. As Fig. 17 and Fig. 18 depict the de-fluoridation amount of both K:R = 0:100 and K:R = 75:25 increase with sintering temperature to the maximum $q_e$ and $Q_m$ at 700 °C before experiencing a sharp drop at around 800 °C. This behavior indicates physical-chemical changes (phase transformations and sintering effect) occurring in the material during sintering. Both PDF analysis and FTIR results indicate that crystallization was more pronounced at 700 °C.

The improvement in de-fluoridation performance as sintering temperature increases (at 500 °C and 700 °C) may be attributed to the formation better de-fluoridating agents such as metal oxides (calcium oxide (CaO) and magnesium oxide (MgO) and beta-tricalcium phosphate ($Ca_3(PO_4)_2$, β-TCP) (possibly, magnesium-substituted beta-tricalcium phosphate, $Ca_{3-x}Mg_x(PO_4)_2$) (Table 8). The formation of these phases result from the decomposition of ACP, pyrophosphates, brushite, OCP and apatites, whose presence is suggested and confirmed by TGA, FTIR and PDF results. It is also worth noting that as the pyrophosphate fraction of the material decreased (FTIR results, Fig. 11 and Table 9), the de-fluoridation performance of the material improved (Fig. 17 and 18). The increase in de-fluoridation performance of the material as pyrophosphate fraction diminishes is consistent with the fact that calcium pyrophosphate is inert towards fluoride (Kocjan, Logar, & Shen, 2017).

Also, literature shows that increase in crystalization leads to a reduction in adsorption capacity (Yakub & Soboyejo, 2013). In this work, increase in β-TCP and metal oxides seem to outweigh

the effect of crystalization at 500 – 700 ℃, leading to increased fluoride removal capacity. The drop of de-fluoridation performance at temperatures between 700 ℃ and 800 ℃ could have been caused by crystalization domination (forming large crystallites) (as indicated by PDF analysis, Fig. 4 and 5). Also, agglomeration, a phenomenon that causes extensive grain growth and reduced surface area (Kocjan *et al.*, 2017), may have occurred (or intensified) at 700-800 ℃, joining forces with crystalization to cause the observed reduction in de-fluoridation performance. In a study by Yakub and Soboyejo (2013), fluoride adsorption data obtained using clay-hydroxylapatite composite adsorbent showed a sharp drop in $Q_m$ at 700 ℃ before rising again at 800 ℃. It was, however, concluded that the de-fluoridation performance of the material (clay-hydroxylapatite composite ceramic) exhibited no clear dependence on sintering temperature. The material prepared in this work (essentially a composite of brushite, ACP, OCP, residue dolostone and apatite before sintering) exhibits a strong dependence on sintering temperature. The difference in phase composition between the calcium phosphate system prepared in this work and one prepared by could be responsible for the difference in displayed de-fluoridation pattern as sintering temperature elevates. Sintered clay material had insignificant de-fluoridation activity in this work.

The maximum de-fluoridation capacity ($Q_m$) of the synthesized clay-Mg/Ca phosphate composite ceramic (K:R = 75:25), sintered at 700 $^oC$ for 8 hours, is 3.2 ± 0.3 mg/g with removal efficiency of up to 96%. When fluoride concentration was increased to 50 mg/L, de-fluoridation capacity increased to 3.8 ± 0.2 mg/g. The $Q_m$ of K:R = 0:100 is 2.6 ± 0.3 mg/g. The higher defluoridation performance of K:R = 75:25 is attributable to the pesence of higher apatite phase content in the material. The higher apatite content in the material K:R = 75:25 is evidenced by the more pronounced dehydroxylation decomposition at 600 – 655 ℃, in K:R = 75:25 (region C and C' Fig. 15) The pH of treated water ranged between 9 and 10.5. Treatment of the material with 0.5 M hydrochloric acid resolved the pH raising problem but reduced $Q_m$ by 30%.

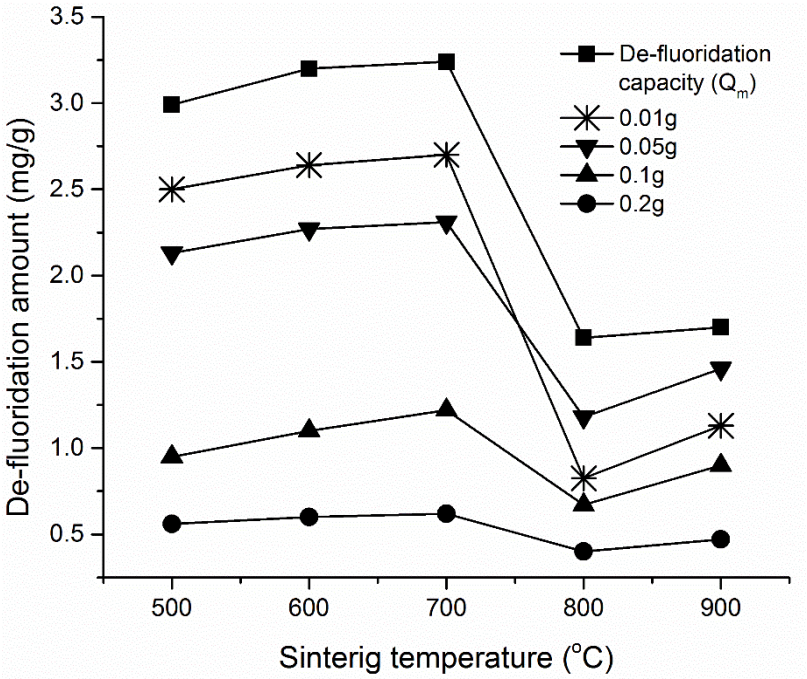


**Figure 17: Shows how de-fluoridation amount varies with material doses as sintering temperature increases at F- concentration of 10 mg/g for K:R = 25:75**

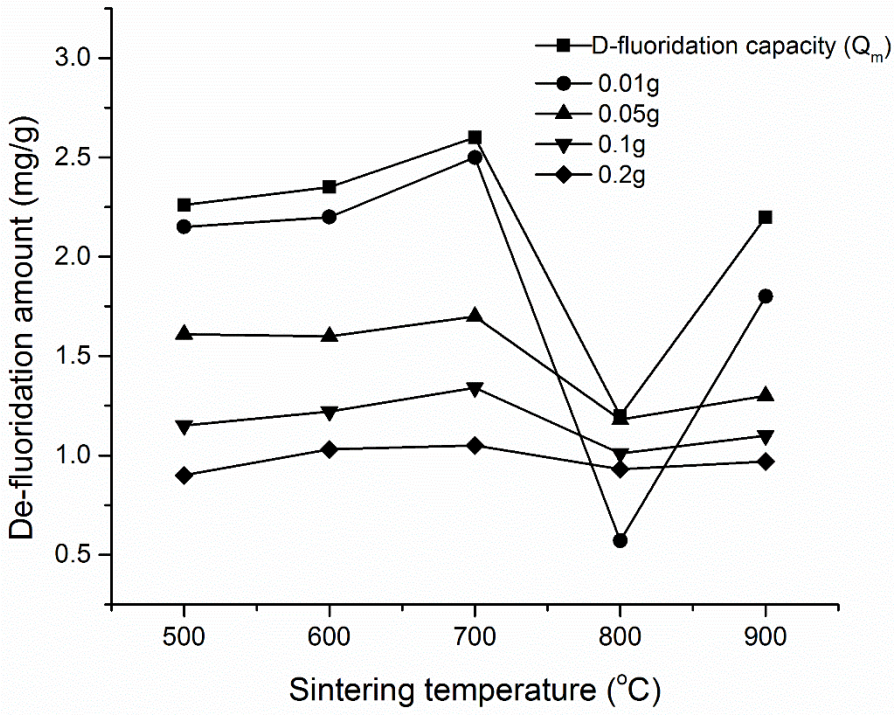


**Figure 18: De-fluoridation amount varies with material doses as sintering temperature increases at $F^-$ concentration of 10 mg/g for K:R = 0:100**

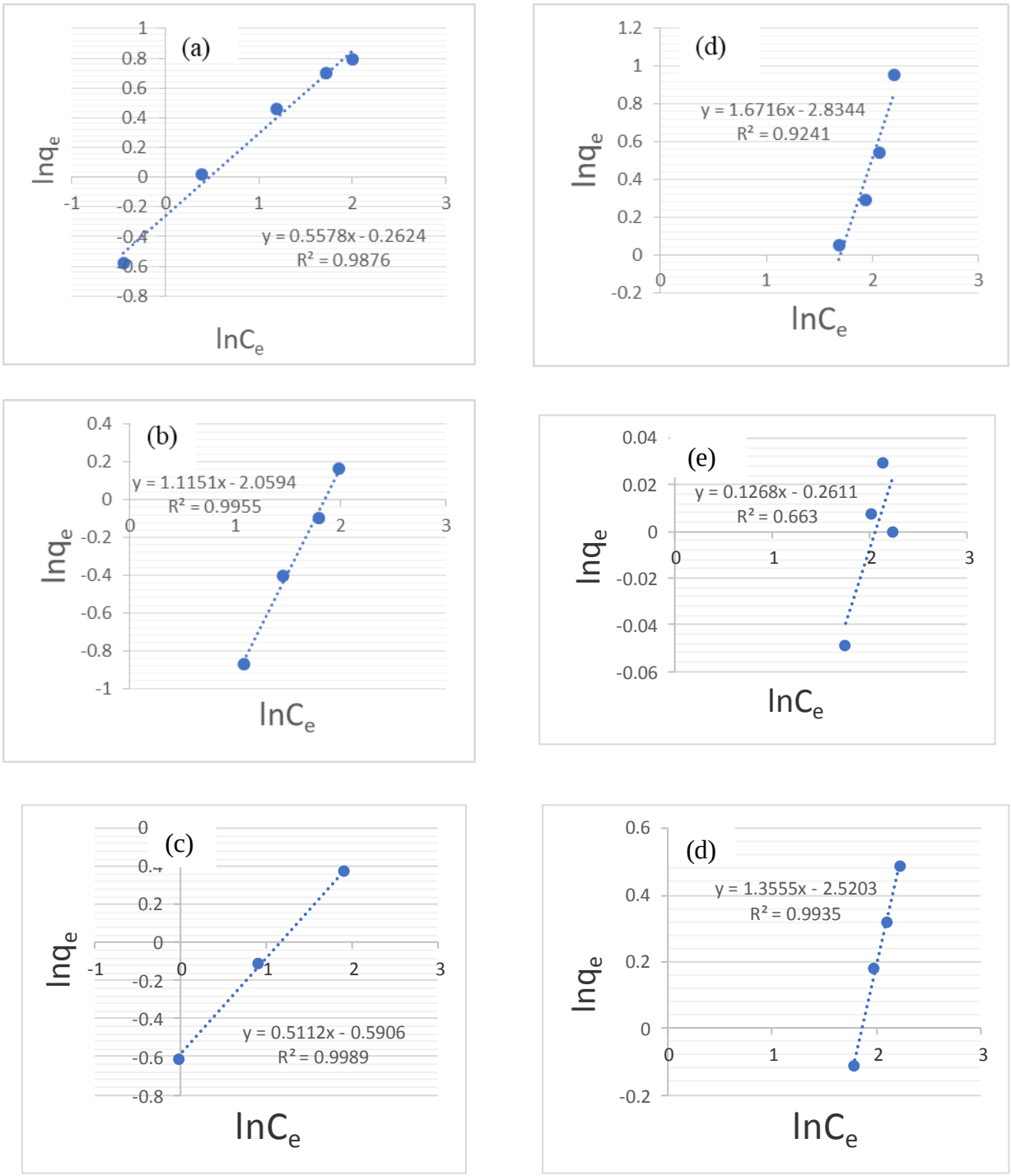


**Figure 19: Selected Freundlich plots to depict de-fluoridation adsorption behavior of K:R = 75:25 sintered at 700 ℃ (a), 800 ℃ (b), 900 ℃ (c) respectively and K:R = 0:100 sintered at 700 ℃ (d), 800 ℃ (e), 900 ℃ (f) respectively**

### 4.4.5 Effect of Initial Concentration

Defluoridation capacity increased as initial concentration was raised. Increasing $F^-$ concentration from 10 mg/l to 50.4 mg/l raised $Q_m$ by ~16.5%. The material R:K = 25:75, at a dose of 0.8 g per 50 mL reduced fluoride from 48 mg/L down to 1.8 mg/g and 3.8 mg/L for

simulated and natural fluoride water respectively. Treatment of natural water with the material raised pH up to10.5 making the water alkaline. Using natural water, it was observed that, the presence of other ions in natural fluoride water had little impact on the de-fluoridation activity of R:K = 75:25 adsorbents sintered at 700 $^{o}$C.

### 4.4.6 Adsorption Kinetics

The fluoride uptake kinetics of the adsorbent K:R = 100:0 and K:R = 25:75, both sintered at 700 ℃, were studied. Figure 20 presents the de-fluoridation amount with respect to time for the two adsorbents. For K:R = 0:100, kinetic results indicate rapid uptake within the first 50 min, reaching > 50% of its equilibrium de-fluoridation amount ($q_e$) at that $F^-$ concentration (10 mg/L). On the other hand, K:R = 75:25 reached over 67% of its $q_e$ in the first 40 min. This shows that clay plays a role in the formation of in-situ formed calcium phosphate.

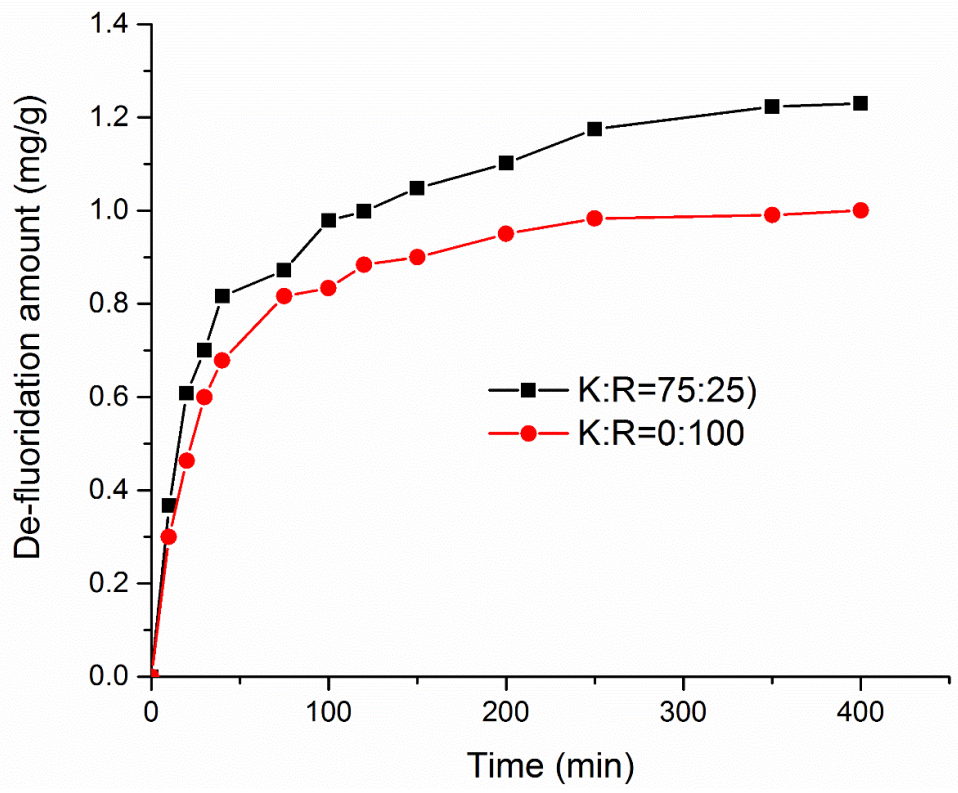


**Figure 20: De-fluoridation amount (mg/g) as a function of time (min)**

To gain insight into the adsorption mechanism, the writers explored the four kinetic models. (Table 12) summarizes kinetic parameters of K:R = 25:75 and R:K = 100:0 sintered at 700 ℃ for the four models tested (Table 1). Figure 21 and 23 represent the plots of the intra-particle diffusion model and pseudo-second order. These two models described the data better. The

intraparticle rate constant, $k_d$ was determined from the slope of stage 2 of the intra-particle diffusion model (Yakub & Soboyejo, 2013). Figure 22 presents stage 2 in Fig. 21.

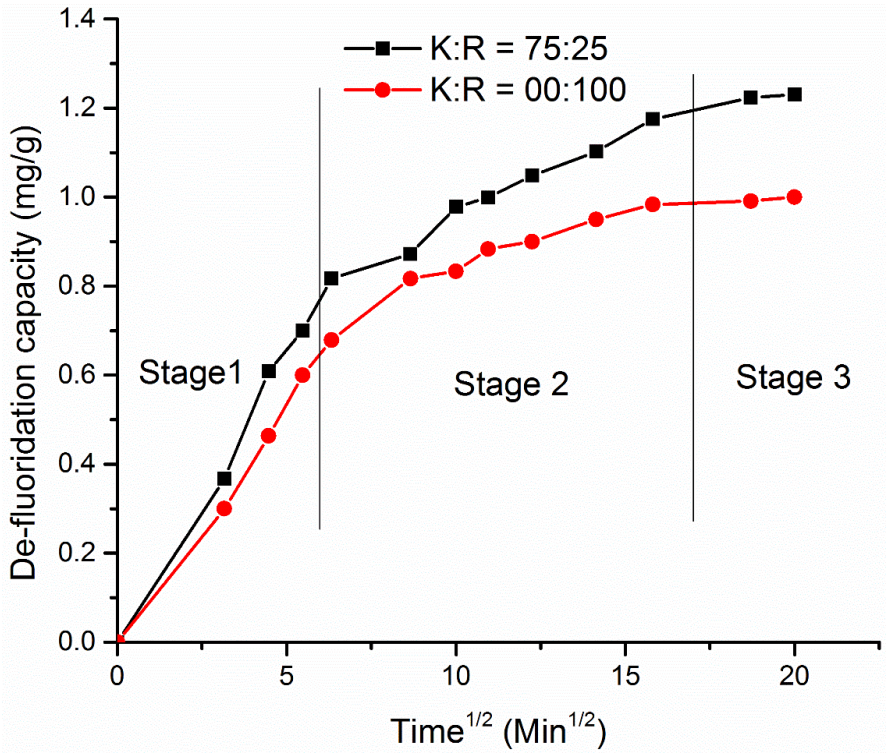


**Figure 21: Intra-particle diffusion model plot showing three distinct kinetic regions**

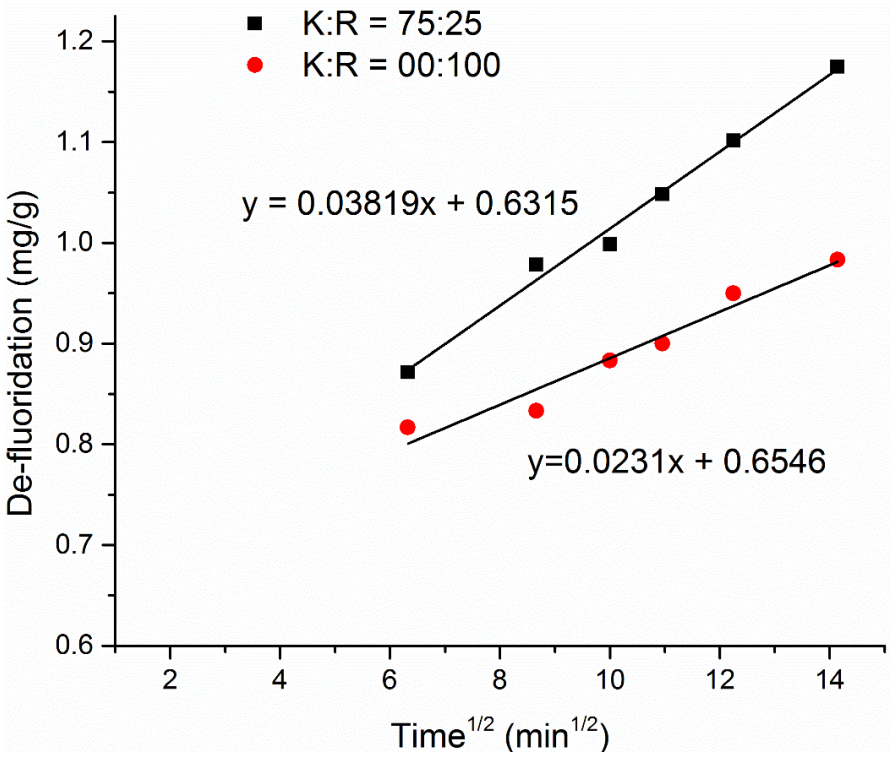


**Figure 22: Region 2 of the intra-particle diffusion mode**

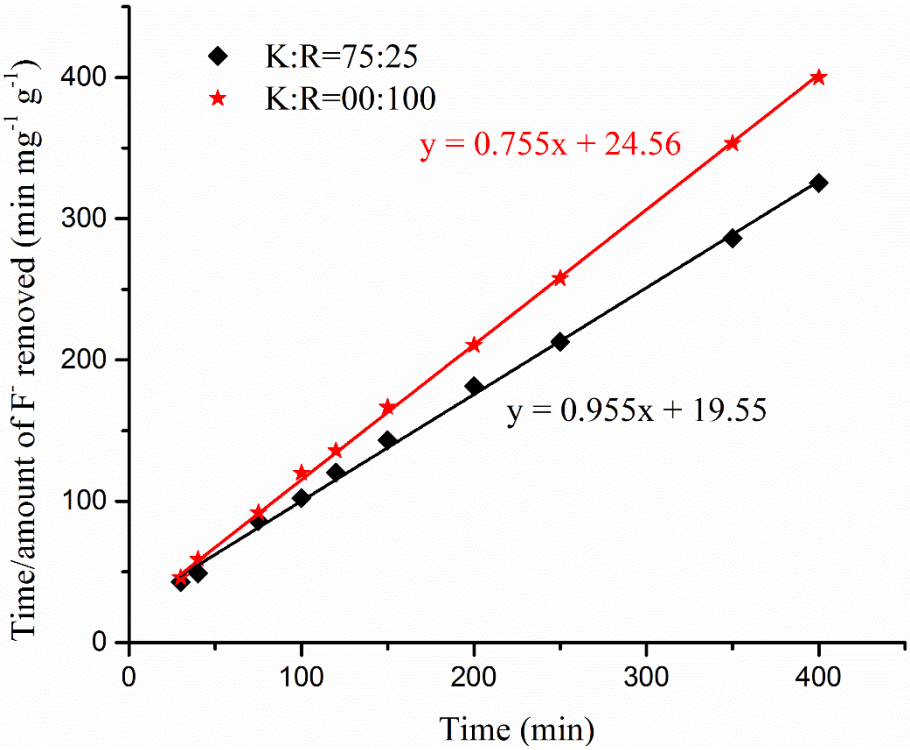


**Figure 23: Pseudo-second model plot**

**Table 12: Kinetic parameters of K:R = 2 5:75 and R:K = 100:0 sintered at 700 ℃**

| Model/Parameter | R:K = 25:75 | R:K = 100:0 |
|---|---|---|
| Particle diffusion model | | |
| $R^2$ | 0.79 | 0.65 |
| $K_p$ ($min^{-1}$) | 0.0029 | 0.0065 |
| C | -0.435 | -0.41 |
| | | |
| Intraparticle diffusion model | | |
| $R^2$ | 0.99 | 0.98 |
| $K_d$ (mg/g $min^{1/2}$) | 0.0391 | 0.0248 |
| C | 0.5746 | 0.5946 |
| | | |
| Pseudo 1st order | | |
| $R^2$ | 0.98 | 0.99 |
| $K_1$ (L/mg) | 0.0106 | 0.0087 |
| $q_e$ calculated (mg/g) | 0.94 | 0.749 |
| $q_e$ experimental (mg/g) | 1.24 | 1.03 |
| | | |
| Pseudo 2nd order | | |
| $R^2$ | 0.99 | 0.99 |
| $K_s$ (g/mg min) | 0.041 | 0.06 |
| $q_e$ calculated (mg/g) | 1.28 | 1.03 |
| $q_e$ experimental (mg/g) | 1.24 | 1.02 |

As can be seen from Table12, $k_d$ values of both K:R = 0:100 and K:R = 75:25 are higher than $k_p$ values. This shows that the intraparticle diffusion model provided a better fit. As indicated by the intra-particle diffusion model fitting (Fig. 21), the adsorption occurs in three stages. The first and rapid stage could be due to bulk diffusion of fluoride ions onto the surface of the adsorbent, whereas the second stage could be due to intraparticle diffusion in the meso- and microporous structures of the adsorbent. The third and slowest stage is the equilibrium. The three stages suggest that the adsorption process is not only a surface phenomenon but also a rate-limiting process in the micro and nano-porous structure (Weber & Morris, 1963). Similar trends have been observed by other researchers (Sundaram, Viswanathan & Meenakshi, 2008b; Yakub & Soboyejo, 2013).

Although $R^2$ of the pseudo-first-order model (0.99 and 0.98 for K:R = 0:100 and K:R = 25:75 respectively) shows good fit (Table 12), the calculated $q_e$ is significantly lower than the experimental values indicating that the model describes the data inadequately. Literature establishes that an adsorption process described by pseudo-first order is inclined towards physisorption (Rodrigues & Silva, 2016; Simonin, 2016). Since pseudo first order model does not describe the data, then physisorption is not the main adsorption mechanism. On the other hand, calculated $q_e$ values extracted from the pseudo-second-order fitting agree well with the experimental values (Table 12). The agreement between the calculated and the experimental $q_e$ values evidences that the pseudo-second-order model describes the adsorption system more adequately than pseudo-first-order. According to literature, an adsorption system that follows pseudo-second order is known to occur by chemisorption (Gosset *et al.*, 1986; Ho, 1995),. Therefore, the materials K:R = 0:100 and K:R = 25:75 removes fluoride by chemisorption process, a process which involves sharing or exchange of electrons between the adsorbate and adsorbent to form a bond(s).

### 4.5 Regeneration of the Material

To test for the renewability (regeneration) of the adsorbent material, 0.1 M sodium hydroxide (NaOH) solution was used as an eluent. The adsorbent was soaked in 50 mL of simulated water containing excess fluoride (200 mg/L) for 24 hours. The fluoride loaded adsorbent was recovered by decantation and washed three times with distilled water. The recovered adsorbent was then soaked in 0.1 M NaOH for three hours and then washed before drying in an oven at 75 ℃ for thee hours. Fluoride was found in the resulting liquor (eluate). Adsorption experiments were then carried out to determine the de-fluoridation capacity of the regenerated adsorbent. This was repeated three times on both R:K = 0:100 and R:K = 25:75. Results showed that the adsorbent R:K = 25:75 lost about 11% of its de-fluoridation capacity after three cycles. On the other hand, the K:R = 0:100 increased its $Q_m$ from 2.8 ± 0.2 mg/g to 3.6 ± 0.3 mg/g after the first cycles. The improved $Q_m$ is possibly due to increase in hydroxylapatite content (a better de-fluoridation agent) which forms when the material is treated with NaOH. In the three circles, the $Q_m$ dropped down to 3.4 ± 0.2 mg/g.

## 4.6 Effect of The Clay-Ca/Mg Phosyphate Composite Ceramic (R:K = 25:75) on Treated Water

To understand the effect of the synthesized clay-Ca/Mg phosyphate composite ceramic (R:K = 25:75) on treated water selected water parameters were measured. Table 13 presents water parameters before and after the treatment of water from Belem spring and Uluwile rivers in Ngarenayuki word, Arusha.

**Table 13: Selected water quality parameters before and after treatment with R:K = 25:75**

| | pH | ORP (mV) | DO (ppm) | EC (µS/cm) | $PO_4^{3-}$ (mg/L) | Hardness (mg/g) | $F^-$ (mg/) |
|---|---|---|---|---|---|---|---|
| Belem spring | | | | | | | |
| Before | 8.7 | 149 | 5.6 | 2698 | 0.1 | 349 | 8.5 |
| After | 10.4 | 162 | 5 | 2728 | 2.6 | 358 | 0.4 |
| Uluwile River | | | | | | | |
| Before | 9.2 | 135 | 4.2 | 1637 | 1.6 | 637 | 48.2 |
| After | 10.5 | 120 | 5.7 | 18770 | 3.2 | 668 | 3.2 |

## 4.7 Fluoride Removal Mechanism

Fluoride uptake mechanisms of calcium phosphate systems have been evaluated by several authors (Sundaram, Viswanathan & Meenakshi, 2008a; Zhang *et al.*, 2012). The main processes are; Ion exchange where fluoride replaces $OH^-$ forming fluorapatite, electrostatic adsorption and precipitation. Since this is a multiphasic material, composed of various phases such as pyrophosphates, apatite, and tricalcium phosphate, various reactions could be responsible for the observed de-fluoridation activity;

### 4.7.1 Magnesium and Carbonate Substituted (type-A) Hydroxylapatite

In addition to electrostatic adsorption, the apatite fraction of the materials removes fluoride through ion exchange (Equation 14)

$$Ca_{5-x}Mg_x(PO_4)_{3-z}(CO_3)_z(OH)_{1-v}V_{v(s)} + F_y^- \rightarrow Ca_{5-x}Mg_x(PO_4)_{3-z}(CO_3)_z(OH)_{1-v-y}V_vF_y^-{}_{(s)} + (OH^-{}^1)_{1-v}(aq) \quad (14)$$

where V is a vacant site induced as a result of substitution

### 4.7.2 Magnesium substituted beta-Tricalcium phosphate

Magnesium substituted beta-tricalcium phosphate dissociate sparingly to release a small number of ions (Equation 15). The released cations, $Ca^{2+}$ and $Mg^{2+}$, react with fluoride ions to form calcium fluoride precipitates (Equation 16 and 17). To maintain the dissociation equilibrium, more of the solid MgβTCP dissociates to replenish the cations (Le Chatelier's principle).

Dissociation reaction

$$Ca_{3-x}Mg_x(PO_4)_{2(S)} \leftrightarrow 2PO_4^{3-} + 3\text{-}xCa^{2+}_{(aq)} + xMg^{2+}_{(aq)} \quad (15)$$

Precipitation (fluoride uptake)

$$Ca^{2+}_{(aq)} + 2F^{-}_{(aq)} \rightarrow CaF_{2(s)} \quad (16)$$

$$Mg^{2+}_{(aq)} + 2F^{-}_{(aq)} \rightarrow MgF_{2(s)} \quad (17)$$

### 4.7.3 Calcium and Magnesium Oxides

Both magnesium and calcium oxides are partially souluble in water forming their hydroxides (Equation 18 and 19). The formed hydroxides react with fluorides to form their respective fluoride salts (precipitation) (Equation 20 and 21).

Dissolution

$$MgO_{(s)} + H_2O_{(l)} \leftrightarrow Mg(OH)_2 \quad (18)$$

$$CaO_{(s)} + H_2O_{(l)} \leftrightarrow Ca(OH)_2 \quad (19)$$

Precipitation (fluoride removal)

$$Ca(OH)_{2(aq)} + 2F^{-}_{(aq)} \rightarrow CaF_{2(s)} + OH^{-}_{(aq)} \quad (20)$$

$$Mg(OH)_2 + 2F^{-}_{(aq)} \rightarrow MgF_{2(s)} + OH^{-}_{(aq)} \quad (21)$$

Magnesium hydroxides have also been reported to adsorb fluoride electrostatically (Devi *et al.*, 2014).

The fluoride uptake mechanisms reviewed here consider only the major metallic elements, magnesium and calcium, and carbonate anion for simplicity. Other anionic and cationic substitutions due to minor elements such as iron, sodium, potassium, barium, sulfate and chlorine may have occurred. Sintered clay showed insignificant de-fluoridation activity.

# CHAPTER FIVE

# CONCLUSION AND RECOMMENDATIONS

## 5.1 Conclusion

Clay ceramic adsorbent materials containing in-situ generated calcium phosphate system was prepared using carbonate rocks as a calcium /magnesium source for water de-fluoridation. This work has demonstrated that heat-pretreated calcitic limestone and dolostone can be used as Ca/Mg source in the synthesis of phosphate composite system with potential application in water purification. It has also shown that clay ceramics (and therefore potentially clay ceramic filters) can be imparted with de-fluoridation capacity/potential by the in-situ generation of Ca/Mg phosphate system. The optimum sintering temperature of the resultant composite, to achieve maximum de-fluoridation capacity, was 700 ℃. At this sintering temperature, the material afforded a maximum theoretical de-fluoridation capacity of 3.8 ± 0.2 mg/g using 48 mg/L fluoride natural water. Defluoridation efficiency of up to 96% was reached at 0.3 g material dosage in less than three hours. The adsorbents exhibit a strong dependence on sintering temperature displaying a pattern where the maximum de-fluoridation performance is achieved sintering temperature of 700 ℃. The adsorption capacity of the adsorbent increases as both fluoride concentration and dolostone content increases when phosphate is proportionally kept constant. The increase in $Q_m$ as sintering temperature elevates, at temperatures between 500 ℃ and 700℃, might be due to the formation of magnesium-substituted tri-calcium phosphate (β-$Ca_{3-y}Mg_y(PO_4)_2$, β-MgTCP) and Cao (as evidenced by the PDF analysis), which outweigh the reduction in $Q_m$ due to increase in crystallinity. At higher temperatures, the de-fluoridation performance drops, possibly due to sintering effect of the material. The Freundlich isotherm model provides a good fit to the obtained experimental data for adsorbents. The adsorption process is found to be non-spontaneous. Furthermore, fluoride ion adsorption follows the pseudo-second-order and intraparticle diffusion model which indicates chemosorption. The method used to synthesize the porous ceramic adsorbent has the potential to be applied in the fabrication of clay ceramic filters which can remove both microbes and fluoride. Preparation of the material at high pH could lead to in-situ formation of phases with higher de-fluoridation activity.

## 5.2 Recommendations

Future studies should focus on studying the mechanical properties of the clay-Ca/Mg phosphate as a function of temperature to establish the optimum sintering temperature and the fabrication of a prototype filter. The adsorbent raised pH of the treated water up to 10.5, giving alkaline water. This may need to be corrected by dipping the ceramic product in alkaline solution and slowly adding dilute phosphoric acid.

## REFERENCES


Agarwal, M., Rai, K., Shrivastav, R., & Dass, S. (2003). Deflouridation of water using amended clay. *Journal of Cleaner Production, 11*(4), 439-444. doi: 10.1016/s0959-6526(02)00065-3

Ajayi, B. A., & Lamidi, Y. D. (2015). Formulation of ceramic water filter composition for the treatment of heavy metals and morrection of physiochemical parameters in household water. *Art and Design Review, 94-100*, 94-100. doi: 10.4236/adr.2015.34013

Ali, I. (2012). New generation adsorbents for water treatment. *Chemical Reviews, 112*(10), 5073-5091. doi: 10.1021/cr300133d

Amini, M., Mueller, K., Abbaspour, K. C., Rosenberg, T., Afyuni, M., Møller, K. N., . . . Johnson, C. A. (2008). Statistical modeling of global geogenic fluoride contamination in groundwaters. *Environmental Science & Technology, 42*(10), 3662-3668. doi: 10.1021/es071958y

Anastasiou, A., Thomson, C. L., Hussain, S. A., Edwards, T. J., Strafford, S., Malinowski, M., . . . Duggal, M. (2016). Sintering of calcium phosphates with a femtosecond pulsed laser for hard tissue engineering. *Materials & Design, 101*, 346-354. doi: 10.1016/j.matdes.2016.03.159

Antonakos, A., Liarokapis, E., & Leventouri, T. (2007). Micro-Raman and FTIR studies of synthetic and natural apatites. *Biomaterials, 28*(19), 3043-3054. doi: 10.1016/j. biomaterials.2007.02.028

Aroke, U., & El-Nafaty, U. (2014). XRF, XRD and FTIR properties and characterization of HDTMA-Br surface modified organo-kaolinite clay. *International Journal of Emerging Technology and Advanced Engineering, 4*(4), 817-825.

Bergaya, F., & Lagaly, G. (2013). General introduction: Clays, clay minerals, and clay science. In B. K. G. T. Faïza Bergaya and Gerhard Lagaly (Ed.), *Handbook of Clay Science: Development in Clay Science* (Vol. 5, pp. pp. 1-19): Elsevier Ltd.

Berzina-Cimdina, L., & Borodajenko, N. (2012). Research of calcium phosphates using Fourier transform infrared spectroscopy. In J. Theophile (Ed.), *Infrared spectroscopy-materials science, engineering and technology* (Vol. 12, pp. 251-263). London, UK: InTechOpen.

Billinge, S. J. (2019). The rise of the X-ray atomic pair distribution function method: A series of fortunate events. *Philosophical Transactions of the Royal Society A, 377*(2147), 20180413. doi: 10.1098/rsta.2018.0413

Bissell, H. J., & Chilingar, G. V. (1967). Classification of sedimentary carbonate rocks. In A. C. M. Rebesco (Ed.), *Developments in sedimentology* (Vol. 9, pp. 87-168): Elsevier.

Boggs J, S., & Boggs, S. (2009). *Petrology of sedimentary rocks* (2nd ed.). Cambridge, UK: Cambridge university press.

Cyriac, B., Balaji, B. K., Satyanarayana, K., & Rai, A. K. (2011). Studies on the use of powdered rocks and minerals for defluoridation of natural water. *Journal of Applied Geochemistry, 13*(1), 62-69.

Dang, T. H., Chen, B. H., & Lee, D. J. (2013). Application of kaolin-based catalysts in biodiesel production via transesterification of vegetable oils in excess methanol. *Bioresource Technology, 145*, 175-181. doi: 10.1016/j.biortech.2012.12.024

Dawley, M. M., Scott, A. M., Hill, F. C., Leszczynski, J., & Orlando, T. M. (2012). Adsorption of formamide on kaolinite surfaces: a combined infrared experimental and theoretical study. *The Journal of Physical Chemistry C, 116*(45), 23981-23991. doi: 10.1021/jp304529n

Desta, M. B. (2013). Batch sorption experiments: Langmuir and Freundlich isotherm studies for the adsorption of textile metal ions onto teff straw (Eragrostis tef) agricultural waste. *Journal of Thermodynamics, 2013*. doi: 10.1155/2013/375830

Devi, R. R., Umlong, I. M., Raul, P. K., Das, B., Banerjee, S., & Singh, L. (2014). Defluoridation of water using nano-magnesium oxide. *Journal of Experimental Nanoscience, 9*(5), 512-524. doi: 10.1080/17458080.2012.675522

Dosen, A., & Giese, R. F. (2011). Thermal decomposition of brushite, CaHPO4· 2H2O to monetite CaHPO4 and the formation of an amorphous phase. *American Mineralogist, 96*(2-3), 368-373. doi: 10.2138/am.2011.3544

Drouet, C. (2013). Apatite formation: Why it may not work as planned, and how to conclusively identify apatite compounds. *BioMed Research International, 2013*, 1-12. doi: 10.1155/2013/490946

Erhuanga, E., Kashim, I. B., & Akinbogun, T. L. (2014). Development of ceramic filters for household water treatment in Nigeria. *Art and Design Review, 2*(01), 6. doi: 10.4236/adr.2014.21002

Fleet, M. E., & Liu, X. (2007). Coupled substitution of type A and B carbonate in sodium-bearing apatite. *Biomaterials, 28*(6), 916-926. doi: 10.1016/j.biomaterials.2006.11. 003

George, S., Mehta, D., & Saharan, V. K. (2018). Application of hydroxyapatite and its modified forms as adsorbents for water defluoridation: An insight into process synthesis. *Reviews in Chemical Engineering*. doi: 10.1515/revce-2017-0101

Gosset, T., Trancart, J. L., & Thévenot, D. R. (1986). Batch metal removal by peat: Kinetics and thermodynamics. *20*(1), 21-26. doi: 10.1016/0043-1354(86)90209-5

Gozalian, A., Behnamghader, A., Daliri, M., & Moshkforoush, A. (2011). Synthesis and thermal behavior of Mg-doped calcium phosphate nanopowders via the sol gel method. *Scientia Iranica, 18*(6), 1614-1622. doi: 10.1016/j.scient.2011.11.014

Gualtieri, A. F., Ferrari, S., Leoni, M., Grathoff, G., Hugo, R., Shatnawi, M., . . . Billinge, S. (2008). Structural characterization of the clay mineral illite-1M. *Journal of Applied Crystallography, 41*(2), 402-415. doi: 10.1107/S0021889808004202

Guggenheim, S., Adams, J., Bain, D., Bergaya, F., Brigatti, M. F., Drits, V., . . . Stanjek, H. (2006). Summary of recommendations of nomenclature committees relevant to clay mineralogy: Report of the association internationale pour l'Etude des argiles (AIPEA) Nomenclature Committee for 2006. *Clays and Clay Minerals, 54*(6), 761-772. doi: 10.1346/CCMN.2007.0550611.

Haerifar, M., & Azizian, S. (2013). Mixed surface reaction and diffusion-controlled kinetic model for adsorption at the solid/solution interface. *The Journal of Physical Chemistry C, 117*(16), 8310-8317. doi: 10.1021/jp401571m

Hauge, S., Österberg, R., Bjorvatn, K., & Selvig, K. (1994). Defluoridation of drinking water with pottery: effect of firing temperature. *European Journal of Oral Sciences, 102*(6), 329-333. doi: 10.1111/j.1600-0722.1994.tb01479.x

Heah, C., Kamarudin, H., Al Bakri, A. M., Bnhussain, M., Luqman, M., Nizar, I. K., . . . Liew, Y. (2012). Study on solids-to-liquid and alkaline activator ratios on kaolin-based geopolymers. *Construction and Building Materials, 35*, 912-922. doi: 10.1016/j.conbuildmat.2012.04.102

Ho, Y. S. (1995). Absorption of heavy metals from waste streams by peat. (Doctoral dissertation, University of Birmingham, Birmingham, United Kingdom). Retrieved from http://etheses.bham.ac.uk/id/eprint/8742

Idini, A., Dore, E., Fancello, D., & Frau, F. (2019). Defluoridation of water through the transformation of octacalcium phosphate into fluorapatite. *Heliyon, 5*(8), e02288. doi: org/10.1016/j.heliyon.2019.e02288

Jovanovski, G., Stefov, V., Šoptrajanov, B., & Boev, B. (2002). Minerals from Macedonia. IV. Discrimination between some carbonate minerals by FTIR spectroscopy. *Journal of Mineralogy and Geochemistry, 177*(3), 241-253. doi: 10.1127/0077-7757/2002/ 0177-0241

Kabir, S., Ahmed, S., Mustafa, A., Ahsan, M., & Islam, S. (2012). Synthesis and characterization of Fe-doped hydroxyapatite. *Bangladesh Journal of Scientific and Industrial Research, 47*(1), 1-8. doi: 10.3329/bjsir.v47i1.10711

Kadir, S., & Akbulut, A. (2009). Mineralogy, geochemistry and genesis of the Taşoluk kaolinite deposits in pre-Early Cambrian metamorphites and Neogene volcanites of Afyonkarahisar, Turkey. *Clay Minerals, 44*(1), 89-112. doi: 10.1180/claymin.2009. 044.1.89

Kanazawa, T., Umegaki, T., & Shiba, S. (1983). Uptake of fluoride ion by amorphous calcium phosphate. *Journal of Chemical Technology and Biotechnology. Chemical Technology, 33*(8), 435-438. doi: 10.1002/jctb.504330808

Karampas, I., & Kontoyannis, C. (2013). Characterization of calcium phosphates mixtures. *Vibrational Spectroscopy, 64,* 126-133. doi: 10.1016/j.vibspec.2012.11.003

Kocjan, A., Logar, M., & Shen, Z. (2017). The agglomeration, coalescence and sliding of nanoparticles, leading to the rapid sintering of zirconia nanoceramics. *Scientific Reports, 7*(1), 2541-.2546. doi: 10.1038/s41598-017-02760-7

Larbi, F., Hamou, A., Bendraoua, A., & Ramdani, N. (2015). Characterization of two natural clays and their application as adsorbents for treatment process of dye effluents. *International Journal of Environmental Monitoring and Analysis, 3,* 10-16. doi: 10.11648/j.ijema.s.2015030501.12

Liu, S. (2015). Cooperative adsorption on solid surfaces. *Journal of Colloid and Interface Science, 450,* 224-238. doi: 10.1016/j.jcis.2015.03.013

Maciejewski, M., Brunner, T. J., Loher, S. F., Stark, W. J., & Baiker, A. (2008). Phase transitions in amorphous calcium phosphates with different Ca/P ratios. *Thermochimica Acta, 468*(1-2), 75-80. doi: 10.1016/j.tca.2007.11.022

Mgbemena, C. O., Ibekwe, N. O., Sukumar, R., & Menon, A. R. (2013). Characterization of kaolin intercalates of oleochemicals derived from rubber seed (Hevea brasiliensis) and tea seed (Camelia sinensis) oils. *Journal of King Saud University-Science, 25*(2), 149-155.

Minh, D. P., Martinez, M. G., Nzihou, A., & Sharrock, P. (2013). Thermal behavior of apatitic calcium phosphates synthesized from calcium carbonate and orthophosphoric acid or potassium dihydrogen orthophosphate. *Journal of Thermal Analysis and Calorimetry, 112*(3), 1145-1155. doi: 10.1007/s10973-012-2695-6

Moore, D. M., & Reynolds Jr, R. C. (1989). X-ray diffraction and the identification and analysis of clay minerals: Oxford University Press (OUP).

Mourabet, M., El Boujaady, H., El Rhilassi, A., Ramdane, H., Bennani-Ziatni, M., El Hamri, R., & Taitai, A. (2011). Defluoridation of water using Brushite: Equilibrium, kinetic and thermodynamic studies. *Desalination, 278*(1-3), 1-9. doi:10.1016/j.desal.2011. 05.068

Murray, H. (1999). Applied clay mineralogy today and tomorrow. *Clay Minerals, 34*(1), 39-49. doi: 10.1180/000985599546055

Nath, S. K., & Dutta, R. K. (2012). Acid-enhanced limestone defluoridation in column reactor using oxalic acid. *Process Safety and Environmental Protection, 90*(1), 65-75. doi: 10.1016/j.psep.2011.07.001

Okada, K., Matsui, S., Isobe, T., Kameshima, Y., & Nakajima, A. (2008). Water-retention properties of porous ceramics prepared from mixtures of allophane and vermiculite for materials to counteract heat island effects. *Ceramics International, 34*(2), 345-350. doi: 10.1016/j.ceramint.2006.10.006

Olaremu, A. G. (2015). Physico-chemical characterization of Akoko mined kaolin clay. *Journal of Minerals and Materials Characterization and Engineering, 3*(05), 353. doi: 10.4236/jmmce.2015.35038

Olejnik, S., Aylmore, L., Posner, A., & Quirk, J. P. (1968). Infrared spectra of kaolin mineral-dimethyl sulfoxide complexes. *The Journal of Physical Chemistry, 72*(1), 241-249. doi: 10.1021/j100847a045

Ombaka, O. (2016). Characterization and classification of clay minerals for potential applications in Rugi Ward, Kenya. *African Journal of Environmental Science and Technology, 10*(11), 415-431. doi: 10.5897/AJEST2016.2184

Pokrovsky, O., Mielczarski, J., Barres, O., & Schott, J. (2000). Surface speciation models of calcite and dolomite/aqueous solution interfaces and their spectroscopic evaluation. *Langmuir, 16*(6), 2677-2688. doi: 10.1021/la980905e

Prekajski, M., Mirković, M., Todorović, B., Matković, A., Marinović-Cincović, M., Luković, J., & Matović, B. (2016). Ouzo effect—New simple nanoemulsion method for synthesis of strontium hydroxyapatite nanospheres. *Journal of the European Ceramic Society, 36*(5), 1293-1298. doi: 10.1016/j.jeurceramsoc.2015.11.045

Rango, T., Vengosh, A., Jeuland, M., Whitford, G. M., & Tekle-Haimanot, R. (2017). Biomarkers of chronic fluoride exposure in groundwater in a highly exposed population. *Science of The Total Environment, 596*, 1-11. doi: 10.1016/j.scitotenv. 2017.04.021

Ren, F. Z., & Leng, Y. (2012). Carbonated apatite, type-A or type-B? *Key Engineering Materials, 493*, 293-297. doi: 10.4028/www.scientific.net/KEM.493-494.293

Robinson, P. (1980). Determination of calcium, magnesium, manganese, strontium, sodium and iron in the carbonate fraction of limestones and dolomites. *Chemical Geology, 28*, 135-146. doi: 10.1016/0009-2541(80)90041-8

Rodrigues, A. E., & Silva, C. M. (2016). What's wrong with Lagergreen pseudo first order model for adsorption kinetics? *Chemical Engineering Journal, 306*, 1138-1142. doi: 10.1016/j.cej.2016.08.055

Sağın, E. U., Böke, H., Aras, N., & Yalçın, Ş. (2012). Determination of CaCO 3 and SiO 2 content in the binders of historic lime mortars. *Materials and Structures, 45*(6), 841-849. doi: 10.1617/s11527-011-9802-1

Sdiri, A., Higashi, T., Hatta, T., Jamoussi, F., & Tase, N. (2010). Mineralogical and spectroscopic characterization, and potential environmental use of limestone from the Abiod formation, Tunisia. *Environmental Earth Sciences, 61*(6), 1275-1287. doi: 10.1007/s12665-010-0450-5

Sempeho, S. I., Kim, H. T., Mubofu, E., Pogrebnoi, A., Shao, G., & Hilonga, A. (2015). Encapsulated urea-Kaolinite Nanocomposite for controlled release fertilizer formulations. *Journal of Chemistry, 2015*. doi: 10.1155/2015/237397

Shiryaev, M., Safronova, T., & Putlyaev, V. (2010). Calcium phosphate powders synthesized from calcium chloride and potassium hydrophosphate. *Journal of Thermal Analysis and Calorimetry, 101*(2), 707-713. doi: 10.1007/s10973-010-0925-3

Shivaraju, H. P., Egumbo, H., Madhusudan, P., Anil Kumar, K., & Midhun, G. (2018). Preparation of affordable and multifunctional clay-based ceramic filter matrix for treatment of drinking water. *Environmental Technology*, 1-11. doi:10.1080/ 09593330.2018.1430853

Sibley, D. F., & Gregg, J. M. (1987). Classification of dolomite rock textures. *Journal of Sedimentary Research, 57*(6), 967-975. doi: 10.1306/212F8CBA-2B24-11D7-8648000102C1865D

Simonin, J.-P. (2016). On the comparison of pseudo-first order and pseudo-second order rate laws in the modeling of adsorption kinetics. *Chemical Engineering Journal, 300*, 254-263. doi: 10.1016/j.cej.2016.04.079

Sobsey, M. D., Stauber, C. E., Casanova, L. M., Brown, J. M., & Elliott, M. A. (2008). Point of use household drinking water filtration: A practical, effective solution for providing sustained access to safe drinking water in the developing world. *Environmental Science & Technology, 42*(12), 4261-4267. doi: 10.1021/es702746n

Somrani, S., Rey, C., & Jemal, M. (2003). Thermal evolution of amorphous tricalcium phosphate. *Journal of Materials Chemistry, 13*(4), 888-892. doi: 10.1039/B210900J

Stanienda-Pilecki, K. J. (2019). The importance of Fourier transform infrared spectroscopy in the Identification of carbonate phases differentiated in magnesium content. *Spectroscopy, 34*(6), 32-42.

Sugiura, Y., & Makita, Y. (2018). Sodium induces octacalcium phosphate formation and enhances its layer structure by affecting the hydrous layer phosphate. *Crystal Growth & Design, 18*(10), 6165-6171. doi: 10.1021/acs.cgd.8b01030

Sundaram, C. S., Viswanathan, N., & Meenakshi, S. (2008a). Defluoridation chemistry of synthetic hydroxyapatite at nano scale: equilibrium and kinetic studies. *Journal of Hazardous Materials, 155*(1-2), 206-215. doi: 10.1016/j.jhazmat.2007.11.048

Sundaram, C. S., Viswanathan, N., & Meenakshi, S. (2008b). Uptake of fluoride by nano-hydroxyapatite/chitosan, a bioinorganic composite. *Bioresource Technology, 99*(17), 8226-8230. doi: 10.1016/j.biortech.2008.03.012

Svinka, R., Svinka, V., Pudze, I., & Damberga, M. (2015). Clay ceramic pellets for water treatment/Mālu keramikas granulas ūdens apstrādei. *Materials Science and Applied Chemistry, 32*(1), 39-44. doi: 10.1515/msac-2015-0007

Theng, B. K. G. (2012). The Clay minerals. In B.K.G. Theng(Ed), *Formation and properties of clay-polymer complexes* (2nd ed). (Vol. 4, pp. 3-37). Amsterdam, The Netherlands: AE: Elsevier.

Toibah, A., Sopyan, I., Yuhazri, Y. M., Jeefferie, R., & Nooririnah, O. (2012). *FTIR study on phase behavior of magnesium-doped biphasic calcium phosphate synthesized via sol-gel method.* Paper presented at the AIP Conference Proceedings 2nd.

Ugolini, F., Dahlgren, R., LaManna, J., Nuhn, W., & Zachara, J. (1991). Mineralogy and weathering processes in recent and holocene tephra deposits of the Pacific Northwest, USA. *Geoderma, 51*(1-4), 277-299. doi: 10.1016/0016-7061(91)90074-4

Valášková, M. (2015). *Clays, clay minerals and cordierite ceramics-A review*. *Ceramics – Silikáty, 59*(4), *331-340*.

Valášková, M., & Martynková, G. S. (2012). Vermiculite: Structural properties and examples of the use. In M. Valaskova (Ed.), *Clay minerals in nature-their characterization, modification and application*. Londan, United Kingdom: IntechOpen.

Vasić, M., Pezo, L., Zdravković, J., Bačkalić, Z., & Radojević, Z. (2017). The study of thermal behavior of montmorillonite and hydromica brick clays in predicting tunnel kiln firing curve. *Construction and Building Materials, 150*, 872-879. doi: 10.1016/j.conbuildmat.2017.06.068

Vecstaudza, J., Gasik, M., & Locs, J. (2019). Amorphous calcium phosphate materials: Formation, structure and thermal behaviour. *Journal of the European Ceramic Society, 39*(4), 1642-1649. doi: 10.1016/j.jeurceramsoc.2018.11.003

Weber, W. J., & Morris, J. C. (1963). Kinetics of adsorption on carbon from solution. *Journal of the Sanitary Engineering Division, 89*(2), 31-60.

William D. Callister, J., & Rethwisch, D. G. (2009). Applications and processing of ceramics. In W. Jennifer, S. Alexandra, F. Janet, N. Hilary, M. Anna, & S. Lauren (Eds.), *Materials Science and Engineering* (8th ed., pp. 501-531). Hoboken, USA: John Wiley & Sons.

Yadav, K. K., Gupta, N., Kumar, V., Khan, S. A., & Kumar, A. (2018). A review of emerging adsorbents and current demand for defluoridation of water: Bright future in water sustainability. *Environment International, 111*, 80-108. doi: 10.1016/j.envint. 2017.11.014

Yakub, I., & Soboyejo, W. (2013). Adsorption of fluoride from water using sintered clay-hydroxyapatite composites. *Journal of Environmental Engineering, 139*(7), 995-1003. doi: 10.1061/(ASCE)EE.1943-7870.0000692

Zereffa, E. A., & Bekalo, T. B. (2017). Clay ceramic filter for water treatment. *Materials Science and Applied Chemistry, 34*(1), 69-74.

Zhang, D., Luo, H., Zheng, L., Wang, K., Li, H., Wang, Y., & Feng, H. (2012). Utilization of waste phosphogypsum to prepare hydroxyapatite nanoparticles and its application towards removal of fluoride from aqueous solution. *Journal of hazardous materials, 241*, 418-426. doi: 10.1016/j.jhazmat.2012.09.066

Zyman, Z. Z., Goncharenko, A. V., & Rokhmistrov, D. V. (2017). Phase evolution during heat treatment of amorphous calcium phosphate derived from fast nitrate synthesis. *Processing and Application of Ceramics, 11*(2), 147-153. doi: 10.2298/PAC1702147Z

# RESEARCH OUTPUTS

**Publication**

**Poster**